

國立交通大學

電子工程學系

電子研究所

碩士論文

砷化銦量子點載子動力學之溫度相依性

Temperature-Dependent Carrier Dynamics of
InAs/GaAs Quantum Dots

研究生：鄭 濬

指導教授：林聖迪 博士

中華民國一〇〇年七月

砷化銦量子點載子動力學之溫度相依性

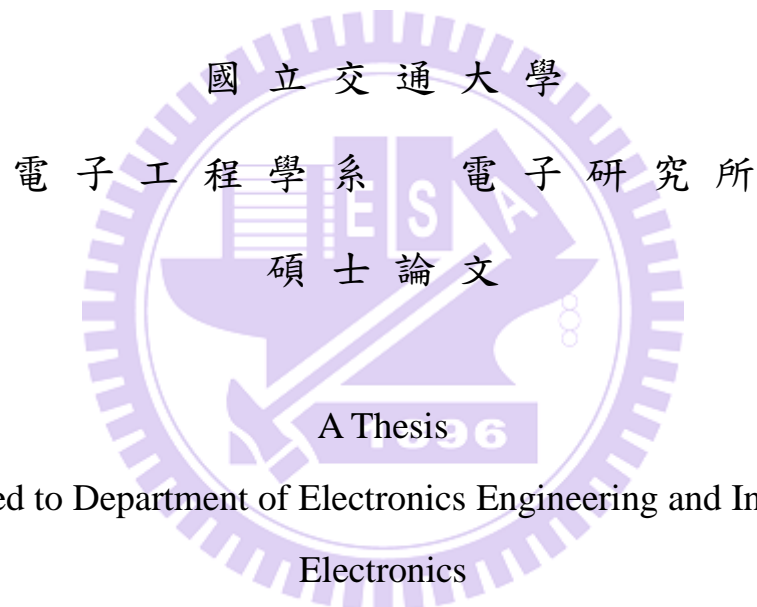
Temperature-Dependent Carrier Dynamics of
InAs/GaAs Quantum Dots

研究生：鄭 濬

Student: Chun Cheng

指導教授：林聖迪 博士

Adviser: Dr. Sheng-Di Lin



Submitted to Department of Electronics Engineering and Institute of
Electronics

College of Electrical and Computer Engineering

National Chiao Tung University

in Partial Fulfillment of the Requirements for Degree of Master in
Electronics Engineering

July 2011

Hsinchu, Taiwan, Republic of China

中華民國一〇〇年七月

砷化銦量子點載子動力學之溫度相依性

學生：鄭 濬

指導教授：林聖迪 博士

國立交通大學

電子工程學系電子研究所碩士班

摘 要

本論文探討成長於砷化鎵基板上之砷化銦量子點中，載子動態行為對溫度的相依性。依據量測變溫的時間解析光譜，在一個小範圍的溫度區間，隨著溫度升高，我們觀察到某些樣品中的光譜從兩段轉變成單一指數衰減的特殊現象，擬合的載子生命期則在某個溫度劇烈的變長爾後又隨著溫度再升高而下降。透過包含了暗態之三態速率方程式模擬，我們推測在低溫時，載子被暗態緩慢的態鬆弛時間所限制而使光譜呈現兩段指數衰減；當溫度升高，額外且速率快的路徑主導了載子傳輸使暗激子快速鬆弛並發光，此時光譜的行為呈現單一指數衰減。此現象說明了欲高溫操作自旋儲存之相關元件，我們必須考慮在高溫時載子藉由額外路徑被快速消耗的機制。

Temperature-Dependent Carrier Dynamics of InAs/GaAs Quantum Dots

Student: Chun Cheng

Adviser: Dr. Sheng-Di Lin

Department of Electronics Engineering & Institute of Electronics
National Chiao Tung University

Abstract

This work focuses on the temperature-dependent carrier dynamics of InAs/GaAs quantum dots. We present an abnormal observation of low-temperature spike on carrier lifetimes caused by the change of decay curves from bi-exponential to mono-exponential decay. Theoretically, we then propose a three-level system containing a dark excitonic state and calculate it with rate equations; we find that at low temperature, the curves behave bi-exponentially due to the slow rate of the spin-flip relaxation of dark excitons; however at higher temperature, carriers are able to relax through an additional path with a much faster rate and the process becomes dominating, leading to the mono-exponential decay curves. The study suggests that to realize high-temperature operation spin storage taking the advantage of dark excitons in QDs, one must consider the fast relaxation through the extra mechanisms favored by thermal energy.

誌 謝

在交大的六年，日子不算短暫，如今即將要在我碩士班畢業畫下一個句點。首先我非常感謝我的指導老師林聖迪老師的指導，在他的帶領下，不管是在學術抑或是做事的方法上，兩年的碩士生涯讓我學到了很多；此外我所待的研究團隊裡，三個指導老師、豐富的資源，還有實力堅強的學長姐，讓我所得到的訓練非常紮實，也很珍惜待在這裡的每一刻。我要特別感謝幾位學長，建宏、大鈞、KB 和小傅，有機會與你們一起共事是很榮幸的，我們總能在討論之中互相學習，我受益良多；我也要謝謝我同屆的好同學們，雖然我們的研究題目是如此的不同，但在平時的生活上，也因為有了你們而增添了许多歡笑及趣事，這將會是我之後點滴的美好回憶。

除了電子研究所帶給我的許多，我要特別提及我大學所就讀的電子物理學系；它帶給了我很好的訓練，讓我在之後研究的學問和方法上能夠很快地上軌道，這是唯有把事情完成後才能深刻體會到的無形力量。謝謝曾經在我大學照顧和指點過我的老師們，我會永遠記得你們。

最後把我的心血獻給我最親愛的父母親和所有的家人，唯有你們在這六年全力的支持，才能夠讓我完成在交大的兩個學位，為之後的更多挑戰做好準備。我由衷的感謝你們的照顧與付出，這是我一生中最大的福氣。我會繼續努力，多看多做，期許自己更上層樓。

Contents

中文摘要.....	i
ABSTRACT.....	ii
誌謝.....	iii
CONTENTS.....	iv
LIST OF FIGURES	vi
LIST OF TABLES	ix
CHAPTER 1 INTRODUCTION.....	1
1.1 A Brief Review.....	1
1.2 Motive – the Temperature Effect	4
CHAPTER 2 SPECTROSCOPY.....	1
2.1 Carrier Dynamics in Semiconductor QDs.....	5
2.2 Steady-State Photoluminescence (SSPL).....	6
2.3 Steady-State Photoluminescence Excitation (SSPLE).....	7
2.4 Time-Resolved Photoluminescence (TRPL).....	8
2.5 Experimental Setup in this Work	12
2.6 Fabrication of InAs QDs Samples.....	15
CHAPTER 3 EXPERIMENTAL OBSERVATION.....	20
3.1 Basic Determinations	20
3.2 Observation of Low-Temperature Spike of Carrier Lifetimes.....	25

3.2.1	Observation and comparison	25
3.2.2	Energy-dependent TRPL	27
3.2.3	Power-dependent TRPL	28
3.2.4	Decay curves of PL intensity.....	29
3.3	The Prolonged Rising Time	32
3.4	Size Dependence of QDs on the Low-Temperature Spike.....	32
3.5	Issues about the Sizes of QDs	37
CHAPTER 4 SIMULATION AND COMPREHENSION		38
4.1	Dark, Bright and Hot States (Excitons).....	38
4.2	Rate Equations.....	41
4.3	Simulation Results.....	43
4.4	Mechanisms – the Effect of Temperature	46
4.4.1	Main discussion.....	46
4.4.2	Discussion on the influences of parameters	50
4.5	Additional Discussions.....	55
4.6	Issues and Limitation	56
CHAPTER 5 CONCLUSIONS AND FUTURE STUDIES		57
BIBLIGRAPHY		59
VITA.....		64

List of Figures

Chapter 1

Figure 1-1: Density of states of (a) bulk, (b) QWs, (c) QWires and (d) QDs.....	2
Figure1-2: Typical morphology on QD structures.....	2
Figure 1-3: Schematic plots of energy levels in the QD system.....	3

Chapter 2

Figure 2-1: Typical procedures for carrier transitions in semiconductor QDs	6
Figure 2-2: Schematic plot of the principle of PL generation.....	7
Figure 2-3: Main principle of the pump-probe technique.....	9
Figure 2-4: Main principle of the streak camera technique	10
Figure 2-5: Main principle of the TCSPC technique	11
Figure 2-6: Final statistical integration of signal in the TCSPC technique	11
Figure 2-7: Schematic plot of the steady-state PL and time-resolved PL system	12
Figure 2-8: Final signal processing of the TRPL measurement.	14
Figure 2-9: Schematic plot of the Stranski-Keastanov mode formation.....	16
Figure 2-10: Comparison of the effective eigenenergies of (a) free particle in a box and (b) QDs.....	17
Figure 2-11: Structure of the InAs QDs studied in this work	18
Figure 2-12: AFM images of all six samples.....	19

Chapter 3

Figure 3-1: SSPL spectra @ T = 25 K of the six samples	21
Figure 3-2: SSPL spectra @ T = 77 K of the four selective samples.....	22
Figure 3-3: (a) Carrier lifetime (τ_1) and (b) PL intensity and FWHM of sample A	24
Figure 3-4: (a) Observation of low-T spike phenomenon in sample C; a typical result is shown in Sample A for comparison. (b) Corresponding integrated PL intensity and FWHM for both two samples.....	26
Figure 3-5: Energy-dependent TRPL measurement of sample A and C	27
Figure 3-6: Power-dependent TRPL of Sample C.....	28
Figure 3-7: Measured decay curves under excitation power of 2 μ W for (a) Sample A and (b) Sample C with their corresponding carrier lifetimes (τ_1).....	30
Figure 3-8: Parameters evaluated from numerical fitting for (a) Sample A and (b) Sample C; (c): comparison of A_2 ratio of sample A and C	31
Figure 3-9: Rising parts of (a) Sample A and (b) Sample C.....	32
Figure 3-10: T-dependent carrier lifetimes (τ_1) for all six samples under 10 μ W	33
Figure 3-11: Measured decay curves of (a) Sample B (b) Sample D (c) Sample E and (d) Sample F with their corresponding τ_1 in the inset figures.....	34
Figure 3-12: Fitting parameters of all six samples. (a) to (d): τ_1 , τ_2 of sample B, D, E and F, respectively; (e): A_2 ratio of all six samples	36
Figure 3-13: (a) SSPL spectra for sample B and C (b) corresponding τ_1 at different temperatures.....	37

Chapter 4

Figure 4-1: Three excitonic states in our model	38
-------------------------------------------------------	----

Figure 4-2: Spin alignments of different kinds of excitons.	39
Figure 4-3: Flow chart of the simulation procedures.....	42
Figure 4-4: Comparison of (a) τ_1 and (b) τ_2 with simulation and experiment	43
Figure 4-5: Decay curves obtained from simulation.....	44
Figure 4-6: A_2 ratio at different temperatures with the corresponding τ_1	44
Figure 4-7: Carrier dynamics at low and high temperatures.....	46
Figure 4-8: τ_{eff} as a function of temperature	48
Figure 4-9: Simplified model with the new introduced parameter τ_{eff}	49
Figure 4-10: Discussions of the parameters: (a) relaxation time from hot to dark state (τ_{hd}) and hot to ground state (τ_{hg}); (b) spin-flip lifetime ($\tau_{spin-flip}$)	51
Figure 4-11: Discussion of the parameters of energy spacing between: (a) hot and dark states (Δ_{hd}); (b) ground and dark states (Δ_{gd}).....	52
Figure 4-12: The influence of initial portion of carriers at ground state	53
Figure 4-13: Simulation result of the rising time.....	54

List of Tables

Table 2-1: Information of the InAs QDs samples 19

Table 3-1: List of peak energies and FWHM of the six samples 19

Table 3-2: List of parameters used for the calculation of injected e-h pairs 23



Chapter 1

Introduction

1.1 A Brief Review

Undoubtedly, III-V semiconductor materials set a decisive milestone in the development of applied photonics in the last few decades. Being very different from single-element semiconductors like silicon and germanium, the direct-bandgap property offers III-V semiconductors a substantial advantage on fabricating optoelectronic devices, bringing about a revolutionary change in our modern society. With the attractive features of ultra-small size and fine output efficiency, commercial products containing semiconductor lasers, light emitting diodes and other related devices are ubiquitous in our daily lives. Moreover, because of the wide variety choices on compound composition, application of higher extent has also been achieved in particular proposes such as infra-photodetectors for thermal imaging [1-4], mid-infrared semiconductor laser for gas detection [5-7], and even high efficiency solar cells [8-11]. In the future, to seek for new inventions and improvement of devices will certainly be one of the most definite targets.

In pursuit of better device performance, researchers have put effort on various emphases including the fundamental improvement on crystal quality and engineering on device structure. Recently, nano-scale structures such as quantum wells (QWs), quantum wires (QWires) and quantum dots (QDs) have intrigued scientists a lot; it is believed that the low-dimensionality of these structures can provide a better carrier confinement and therefore leads to significant improvement on device performance.

Among so many options, QDs have recently caught considerable attention for the three-dimensional quantization which results ultimately strong carrier confinement.

Fig. 1.1 shows the comparison of density of states (DOS) of bulk, QWs, QWires and QDs. The zero-dimensionality of QDs leads to a δ -like DOS [12], meaning both electrons and holes are spatially restricted in all dimensions and have only particular allowed states to occupy. Therefore, the property is exactly suitable for optoelectronic devices and researchers have worked greatly on this candidate structure.

To conceptually introduce the QD system, we show a typical morphology on QD ensembles in Fig. 1-2, and the discrete-energy levels in QDs are also schematically plotted in Fig. 1-3; notice that the meanings of the symbols are mentioned in the figure caption. In addition to the relatively lower ground and excited states, there exists some *quantized* but quasi-continuous levels with higher energies but very small energy spacing due to the junction between QD and the two-dimensional matrix material. Furthermore, for the larger effective mass of holes, the energy levels in valence band (V.B.) are smaller than the ones in conduction band (C.B.).

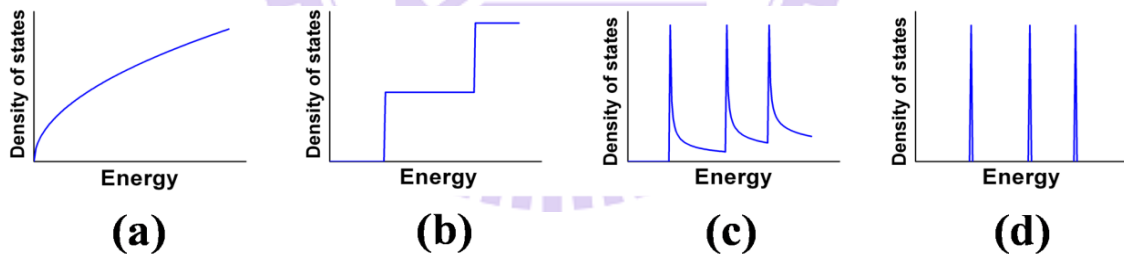


Figure 1-1: Density of states of (a) bulk, (b) QWs, (c) QWires and (d) QDs.

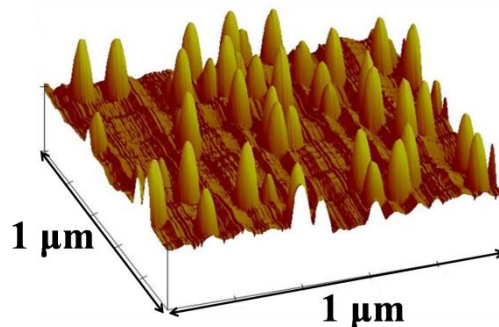


Figure 1-2: Typical morphology on QD structures.

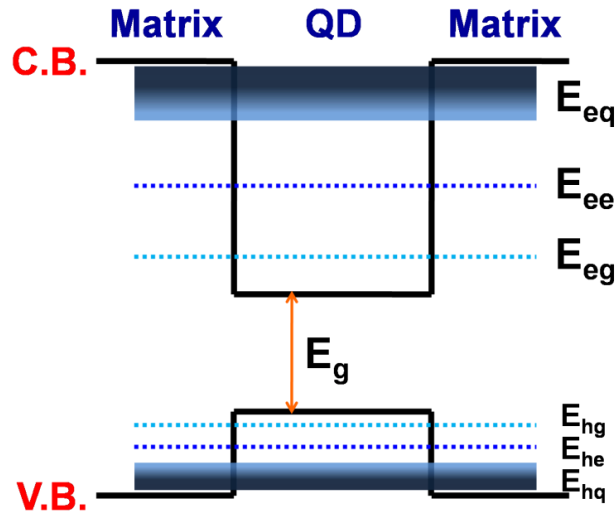


Figure 1-3: Schematic plots of energy levels in the QD system. Symbols: E_g : bandgap energy; $E_{e(h)g}$: ground state energy of electron (hole); $E_{e(h)e}$: excited state energy of electron (hole); $E_{e(h)q}$: quasi-continuous state energy of electron (hole).

Within many QDs with different materials, In(Ga)As QDs are so attractive due to the benefit on easy fabrication on matured-studied GaAs system. There are many demonstrations about the great characteristics of InAs QD-based devices such as the lower threshold current of laser diodes [13-15] and higher operation temperature of infrared photodetectors [1, 2]; also, it provides a great opportunity for tuning the emission wavelength to telecommunication range [16]. On the other hand, it has been shown that InAs QDs can be used as devices of quantum photonics like single photon emitters, being a tempting choice for the use of quantum information processing [17-19].

1.2 Motive – The Temperature Effect

In order to further realize the room temperature operation for advanced QD-based devices, an indispensable work of understanding the temperature effect on the QD systems turns out to be necessary. As non-zero thermal energy being naturally inevitable, we must factor in its influence as considering both the device performance and reliability; it is especially more crucial for devices fabricated with quantum structures since the related energy of the systems is often in the order of eV, or even smaller to be meV; therefore, the investigation of temperature effect remains one of the most valuable topics in studying semiconductor QDs.

As a matter of fact, the role of temperature has been widely studied from different aspects. For instance, there are discussions which focus on the temperature effect directly on device operation [20, 21]. As for the researches on mechanisms, non-radiative recombination at high temperature being an unwanted path to deplete carriers is demonstrated to be significant in self-assembled QDs [22-24]; also, both steady-state and time-resolved studies show that carrier distribution will form local equilibrium among QDs as temperature rises [23, 25-27], and quantum tunneling is as well shown to be favored by thermal energy [28]. Moreover, the thermalized carriers can undergo intraband transition [29], and even populate optically inactive states which results an increase in carrier lifetimes of QDs [30]. The observation of these phenomena let us further picture the world of QDs and we accordingly carry out the study of this work.

Chapter 2

Spectroscopy

Before entering our main studies, we give essential introductions to the spectroscopy techniques and InAs QDs samples studied in this work. The spectroscopy covers steady-state and time-resolved determinations, where the two both give important information but from different aspects. On the other hand, the structure and morphology of the six studied samples are introduced so that one can have the central view on the InAs QDs in our study.

2.1 Carrier Dynamics in Semiconductor QDs

When it comes to direct-bandgap semiconductors, the luminescence spectroscopy remains one of the most important approaches to investigate the intrinsic behaviors of carriers in the system interested, and the behaviors are so worth studying since they are the key principles closely related to further device operation.

Fig. 2-1 schematically shows the three major procedures of carrier dynamics in QDs when electron-hole pairs (excitons) are generated by an external excitation: capture, relaxation and recombination. After firstly captured by QDs, carriers may undergo a rather fast process to *relax* from higher quantum states to lower ones with the emission of phonons; also, the separated electrons and holes may have a chance to *recombine*, in this case, generating photons. Studies have found that the rate of relaxation and recombination process are usually quite different, typically being in the order of ps^{-1} and ns^{-1} [31, 32], respectively. It consequently explains that fact that recombination often takes place after carrier relaxation.

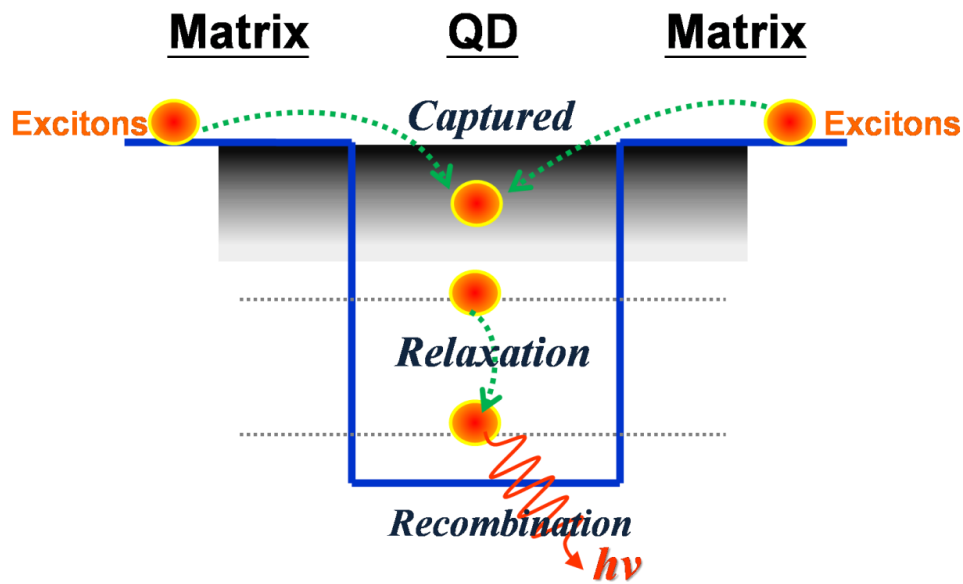


Figure 2-1: Typical procedures for carrier transitions in semiconductor QDs.

2.2 Steady-State Photoluminescence (SSPL)

The steady-state luminescence spectrum is the fundamental spectroscopy for semiconductors which determines the energies of the emission photons generated from the recombination process. As shown in Fig. 2-2, photons with energy higher than the one of band gap (E_g) are input to pump the electrons from V.B. to C.B.; the holes and electrons relax to lower states and then recombine to generate PL. For the measurement of this kind, the detection focuses on different luminescence energies and is in *steady-state* condition. The excitation will generally be a photon source such as a laser because of the experimental convenience, giving the name to the analysis as *photoluminescence*; however, the excitation source can vary to be others like a bias voltage (*electroluminescence*) or a cathode source (*cathodeluminescence*).

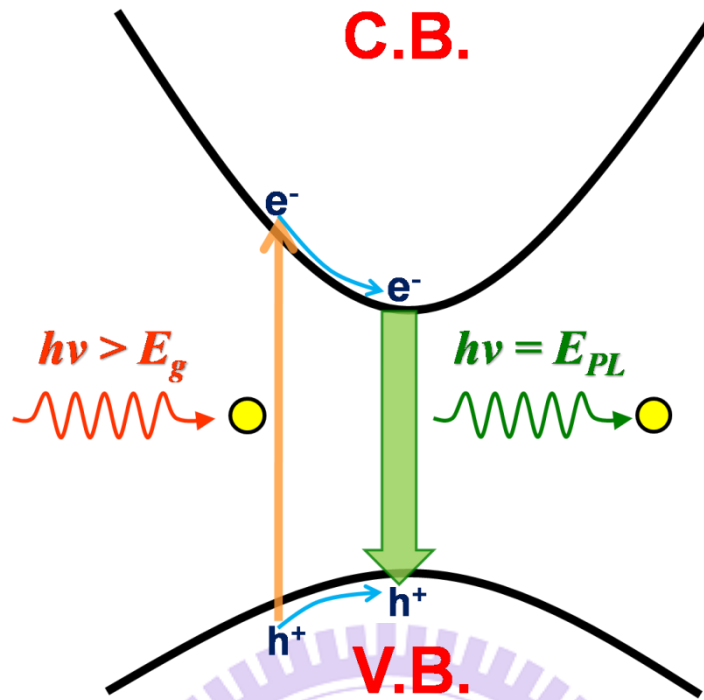


Figure 2-2: Schematic plot of the principle of PL generation.

2.3 Steady-State Photoluminescence Excitation (SSPLE)

In addition to SSPL, the SSPLE is another useful steady-state spectroscopy to determine the energy levels in nano-structures. The major difference between the SSPL and SSPLE is the energy of the excitation source (laser). For SSPL, the photon energy of the laser is usually fixed while in SSPLE an *energy-tunable* photon source is used. It is well known that the input photons will only be absorbed by electrons in valence band to jump to conduction band when the energy of the input photons matches the energy difference between the two quantum states. Therefore, we can determine the energy levels by varying the energy of the input photon and monitor the PL intensity.

2.4 Time-Resolved Photoluminescence (TRPL)

Unlike steady state measurement whose spectrum is resolved in *frequency* domain, time resolved photoluminescence deals with the spectroscopy in *time* domain, or the time dependence of photon generation. Imagine a specially-made ball whose color will change every millisecond. If one wishes to record all the colors that it reveals within a long time interval by a camera, the time interval between two shots of the camera must be less than one millisecond, or otherwise, some information will definitely be lost. Similarly, only by using a detection method with detection speed faster than it of the dynamic event itself can we ensure that the dynamic behaviors are completely recorded. In order to detect the event of carrier relaxation (picosecond order) and recombination (nanosecond order), the time resolution of the measurement techniques must be at least comparable (or faster) to them. Here we introduce the main principles of the three most commonly used methods for studying time-resolved spectroscopy in semiconductor nanostructures.

Pump-probe spectroscopy

The pump-probe spectroscopy is basically the application of optics. As shown in Fig. 2-3, a laser pulse is initially divided into two, the “pump” and “probe” beams, and a time delay Δt will be deliberately given between the two; the pump beam is targeted to excite the sample, while the other is used for probing the dynamic signal which will be collected by a detector. By adjusting Δt , one can get the time-dependent spectrum, which can be reflectivity, absorption or luminescence.

A commanding advantage of this approach will be the time resolution; ideally, its resolution is only determined by the pulse width of the laser [33], and by using the

laser with ultra-short pulse width, one can easily reach to an ultra-fast detection capability of femtosecond order or even higher.

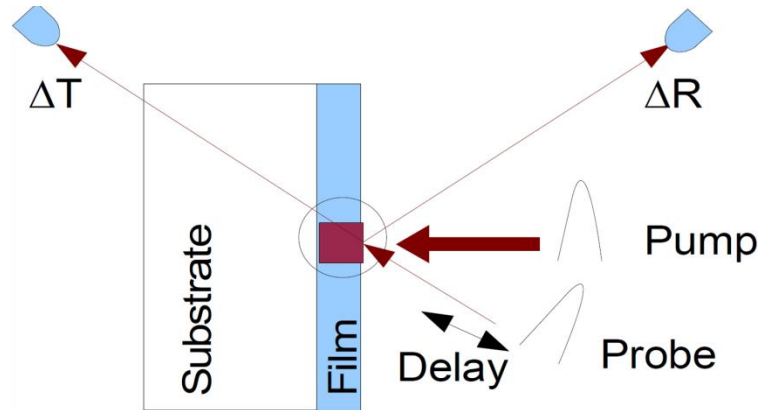


Figure 2-3: Main principle of the pump-probe technique.
(Source: Z. Sun, "Time Resolved Pump-Probe Spectroscopy.")

Streak Camera^[34]

A typical streak camera system is shown in Fig. 2-4. The signal generated by the sample will be focused to one photocathode to excite photoelectrons. The photoelectrons then are accelerated by an ultra high voltage to enter the sweep field, which provides a time-varying voltage. Finally the photoelectrons are reached on a screen for detection.

With this approach, one can directly get the data in a large detection range and it is very useful in some research aspects. Nonetheless, its time resolution can only be reached to the order of picosecond due to the limitation of the sweep rate of electronic devices.

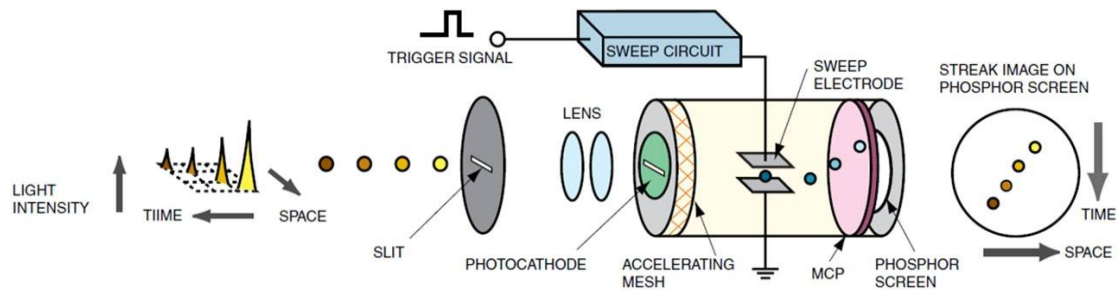


Figure 2-4: Main principle of the streak camera technique.

(Source: "Guide to Streak Cameras," Hamamatsu Photonics.)

Time Correlated Single Photon Counting ^[35]

The major principle of Time Correlated Single Photon Counting (TCSPC) is a fairly smart one, mainly making use of the concept of statistics. Referring to Fig. 2-5, the measurement is proceeded by *averagely allowing one or no photon* between two laser pulses. When a photon appears, the time interval (Δt) will be recorded to complete a detection event, and the procedure will carry on repeatedly. Although Δt may be different from every event, one can get a statistically reliable result after a large quantity of repeated detections, as shown in Fig. 2-6.

Generally, the time resolution of TCSPC method can be reached to the order of picosecond, usually limited by the speed of the detectors. A great advantage about TCSPC method is the capability of detecting signal with low intensity by choosing suitable detectors such as photomultipliers (PMTs) or avalanche photodiodes (APDs); furthermore, the system is quite simple so that it is possible to additionally assemble it on the existing-experimental system by only adding several instruments.

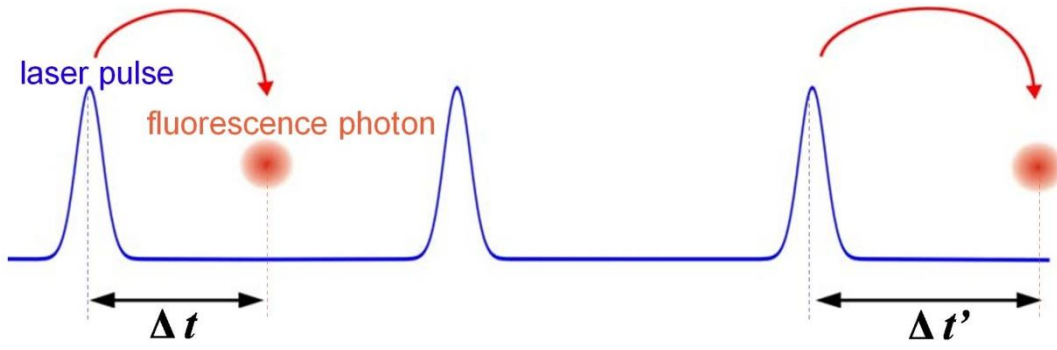


Figure 2-5: Main principle of the TCSPC technique.

(Source: Reference. 35.)

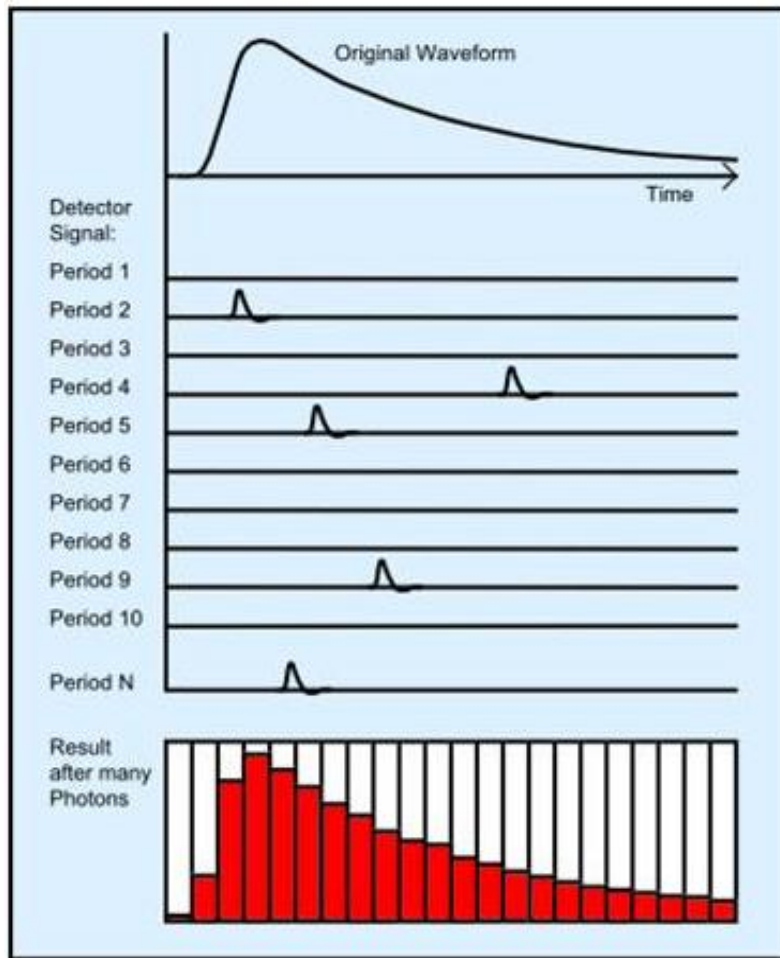


Figure 2-6: Final statistical integration of signal in the TCSPC technique.

(Source: W. Becker, A. Bergmann, "Detectors for High-Speed Photon Counting.")

2.5 Experimental Setup in This Work

Steady-state PL

The steady-state luminescence spectra are obtained by PL in this work, and the apparatus is schematically drawn in Fig. 2-7. The sample is placed in a low-temperature (low-T) chamber with a closed-cycled helium cryostat used for temperature control; to increase the signal-to-noise ratio, a chopper and lock-in amplifier are applied. A diode laser (PicoQuant LDH-P-780, peak wavelength at 780 nm) is used as an external excitation source, and after passing through few reflection mirrors, the laser hits the sample and makes it generate spontaneous emission to be focused back by another two lens into a monochromator (JobinYvon iHR-550). The luminescence is then resolved by a 1200 gr/mm grating and collected by an InGaAs solid-state detector whose response wavelength is from about 800 to 1500 nm (near infrared). Notice that the monochromator carries two exits and a guiding mirror is arranged to guide the light entering one of them.

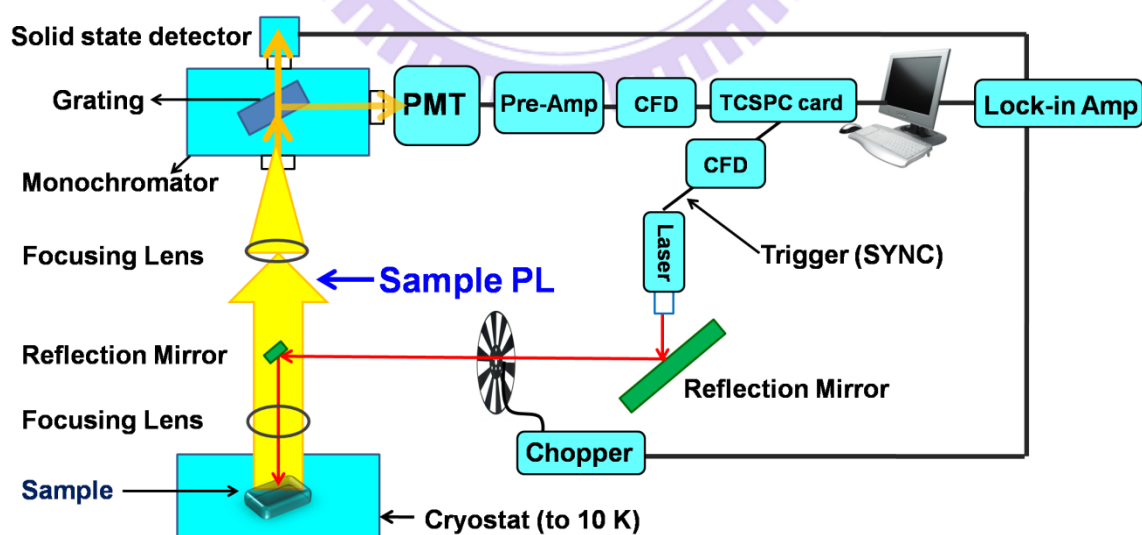


Figure 2-7: Schematic plot of the steady-state PL and time-resolved PL system.

Time-resolved PL

The TRPL measurement is carried out by the TCSPC technique mentioned in the last chapter. The system is assembled additionally on the original set-up of the SSPL and the two actually share many common apparatus. The same diode laser is used for excitation except that the repetition rate is kept at 10 MHz in TRPL measurement while it is irrelevant in steady-state PL; moreover, both the laser beam and emitted luminescence undergo the same optical alignment as in the steady-state situation. As for the different aspects, first, the chopper and lock-in amplifier are not used and because of the *dynamic* measurement of TRPL, the detector must be able to “count” the signal as well, so an InGaAs photomultiplier tube (PMT, Hamamatsu H10330-75) is applied here. After selecting the detected wavelength, the guiding mirror in the monochromator is set to guide the light to the exit facing the PMT. Another difference resides in the final signal processing done by many delicate electronic devices, introduced as follows.

Beside the general laser beam used for excitation, an additional pulse signal is sent as a synchronization (SYNC) trigger and directly enters a constant fractional discriminator (CFD) to be a reference signal; the CFD acts as a threshold level to filter out the noise and judge whether the signal is valid. On the other hand, the luminescence signal will be detected by the PMT and then magnified by a pre-amplifier before entering the CFD. In the end, both signals enter the TCSPC counting card (Time Harp 200) for final statistical integration, as shown in Fig. 2-7, too.

The framed part in Fig. 2-8 shows that the TCSPC counting card can be further divided into three components, the time-to-amplitude converter (TAC), analog-to-digital converter (ADC) and histogrammer. As the TAC detects the signal, the embedded capacitance starts to charge till the next SYNC trigger. The ADC then

transforms the charge (voltage) signal to digital information of time to be inputted into the histogrammer. At this moment, one detection event is completed, and with numerous times of integration, one can get the time-dependent luminescence intensity like the one in Fig. 2-6.

Due to the system resolution is limited to be about 300 ps, it is only enough to detect the recombination dynamics but incapable for the relaxation. In other words, only the *decay* parts in the curves (Fig. 2-6) have the quantitative meaning whereas the *rising* will reveal merely the system resolution. For numerical fitting, we apply a bi-exponential decay function to evaluate the carrier lifetimes

$$I_{PL}(t) = A_1 \exp(-t/\tau_1) + A_2 \exp(-t/\tau_2) \quad (2-1)$$

We define the smaller and larger lifetimes to be respectively τ_1 and τ_2 , and τ_1 (i.e. the faster part) will be focused in the following discussion unless exceptionally mentioned.

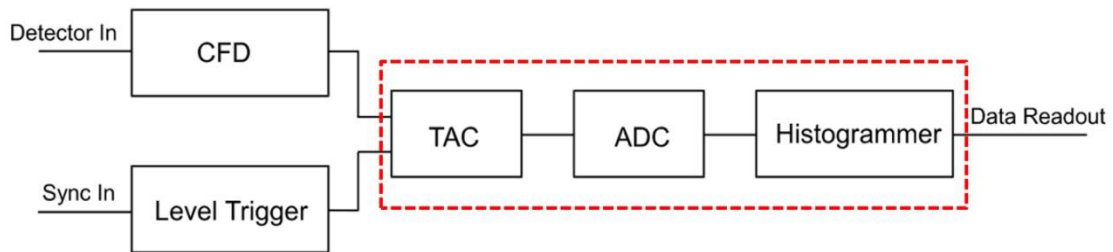


Figure 2-8: Final signal processing of the TRPL measurement. (Framed part: The electronic devices inside the TCSPC card.)

(Source: W. Becker, A. Bergmann, "Detectors for High-Speed Photon Counting.")

2.6 Fabrication of InAs QDs Samples

It cannot be overemphasized the essentiality of epitaxy in fabricating semiconductor nanostructures; if the crystal quality of the sample were already poor, the following study or further processed device would turn out to be in vain because of its natural imperfections. For instance, the interference of non-ideal effects due to poor crystal quality shall mask the original phenomena from our observation, not to mention its negative influence on device performance. Therefore, researchers have worked hard in these decades to improve the epitaxy techniques and have made a superior progress, including novel mechanical inventions such as molecular beam epitaxy (MBE) and metal organic chemical vapor deposition (MOCVD); nowadays, not only can we get samples with fine quality but many novel structures and materials can be put into new attempt.

The Stranski – Keastanov method ^[14, 36, 37]

To fabricate semiconductor QDs, the Stranski-Keastanov mode (S-K mode) epitaxy offers a reliable and convenient way. As shown in Fig. 2-9, a thin wetting layer is firstly deposited on a barrier layer (or simply a substrate); due to the lattice mismatch between the barrier and epitaxial material, strain quickly starts to pile up in the system; it is not until the critical moment that the structure can no longer sustain the accumulation of strain does the two-dimensional surface stop forming, changing into island or point-like shape to partially release energy of the system, and QDs are formed under this circumstance. A major key for this dimensional transition to occur is that the degree of lattice mismatch must be large enough for the two materials, for example, 7.2 % for InAs and GaAs; in addition, for its spontaneous relaxation of strain to form the structure, it is also named as “self-assembled” formation.

The S-K mode approach has been widely applied in the growth of different nano-structures for both its uncomplicated procedures and capability for large number of output elements in one growth period.

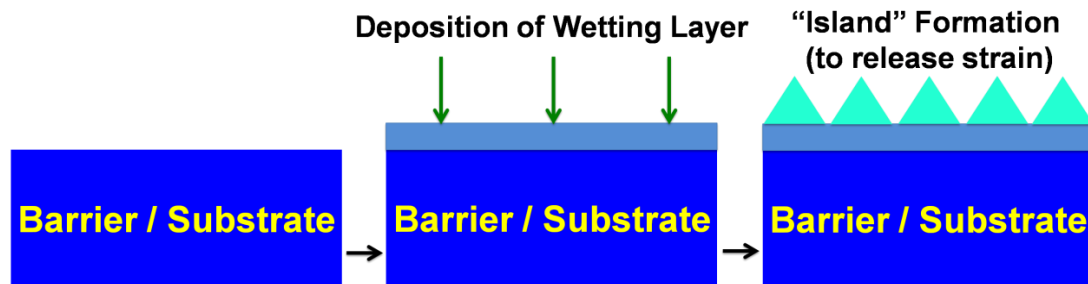


Figure 2-9: Schematic plot of the Stranski-Krastanov mode formation.

Quantized Energies of QDs

By varying the epitaxial conditions, we can control the size of the formed QDs, which is closely related to their intrinsic energy levels. Let us first recall a simple case. For a free particle inside a one-dimensional box of length L with infinite potential confinement, it is well-known that its ground state energy is inversely proportional to L^2 , so is and the energy spacing between ground and first excited state. Qualitatively speaking, the energy and energy spacing will both be higher as long as the length of the box is shorter (Fig. 2-10(a)).

In fact, the case in QDs have a good analogy since it provides just a strong potential well for confining carriers, where the energy and energy spacing are higher (lower) for smaller (larger) QDs, as shown in Fig. 2-10 (b). However, except the size of QDs, there are still other factors which determine the energy levels such as the intermixing of matrix and QD materials; for just a gradual view and simplicity, we treat the energy level and energy spacing to be *effectively* higher (lower) as the size of QDs is smaller (larger) in this study.

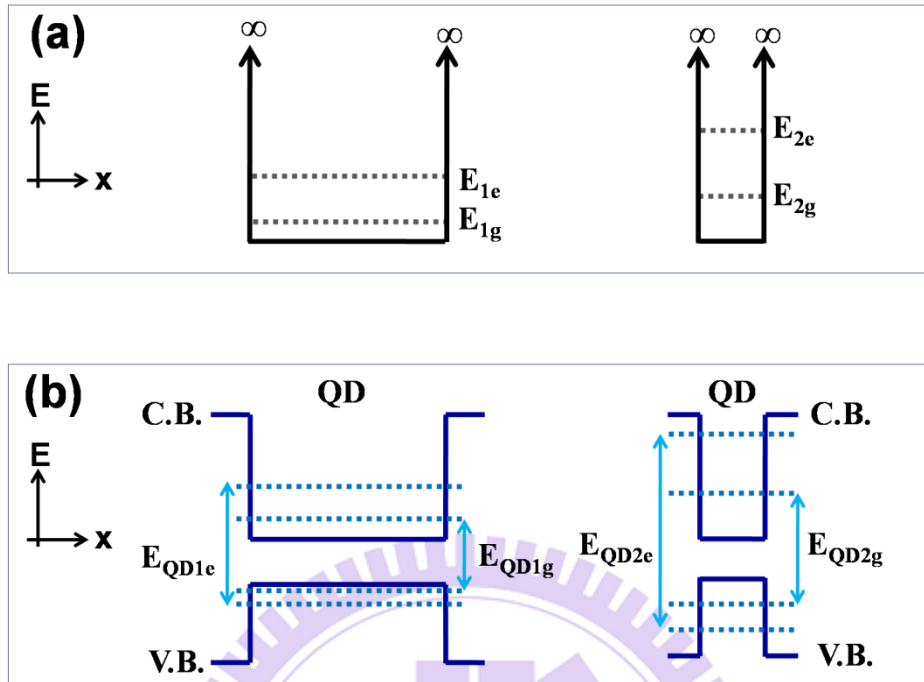


Figure 2-10: Comparison of the effective eigenenergies of (a) free particle in a box and (b) QDs. For the two different sizes of QDs, we show the energy $E_{QD2g(e)} > E_{QD2g(e)}$, and also $(E_{QD2e} - E_{QD2g}) > (E_{QD1e} - E_{QD1g})$.

Sample structure

Six self-assembled InAs QDs samples grown by MBE on (100) GaAs substrate are studied in this work; their structures are basically the same shown in Fig. 2-11. A relatively thick GaAs buffer layer is firstly deposited on the substrate; the self-assembled QDs were embedded in GaAs matrix and sandwiched with Al(Ga)As confinement layers. Finally, uncapped QDs were grown on the surface with the same growth conditions of the embedded ones for morphology measurement. In addition, the QDs layer of the six samples were grown under different growth temperatures and deposited monolayers (MLs), leading to the QDs with both different densities and sizes.

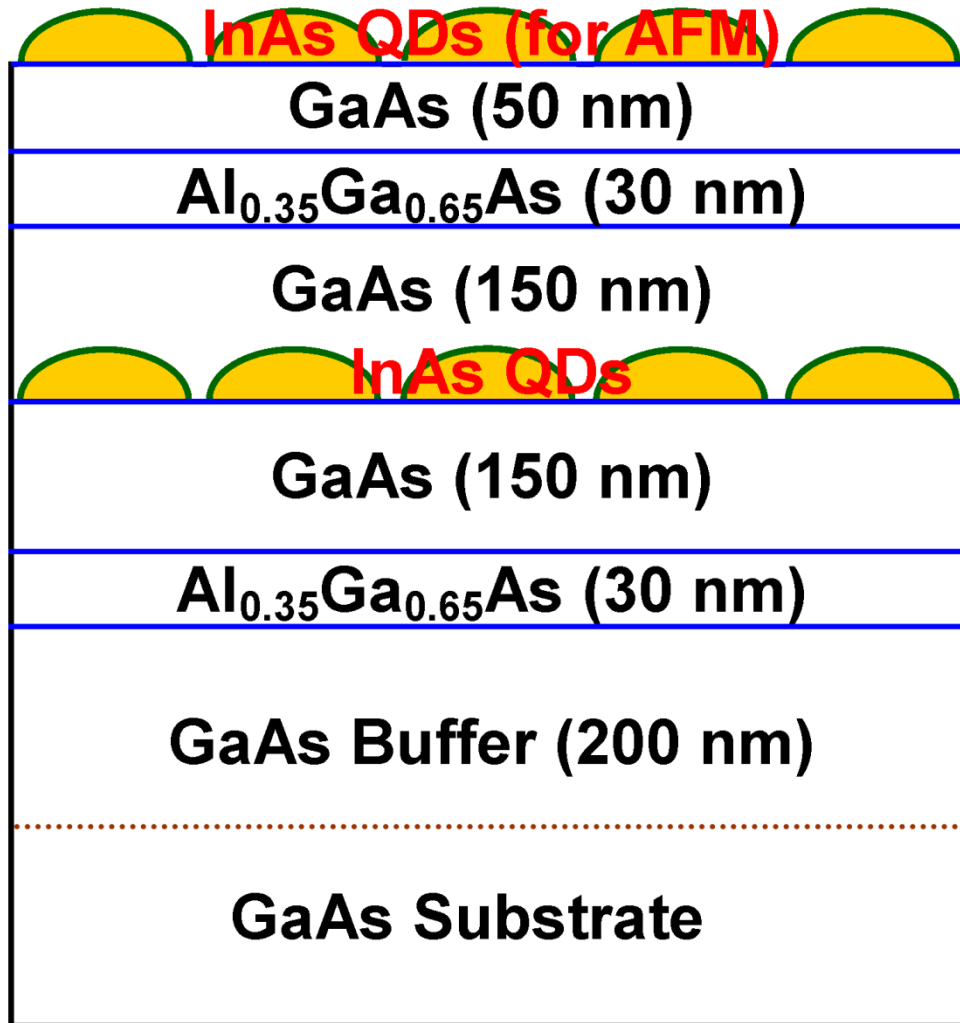


Figure 2-11: Structure of the InAs QDs studied in this work.

Morphology

The morphology measurement is done by using atomic force microscopy (AFM), one of the most powerful methods for obtaining surface information. The AFM of the six samples are shown in Fig. 2-12 (a) to 2-12 (f) with the scale of $1 \times 1 \mu\text{m}^2$. For simple comparison, information including growth conditions, average QD density (D) width, height, and the corresponding sample numbers are all listed in Table 2-1.

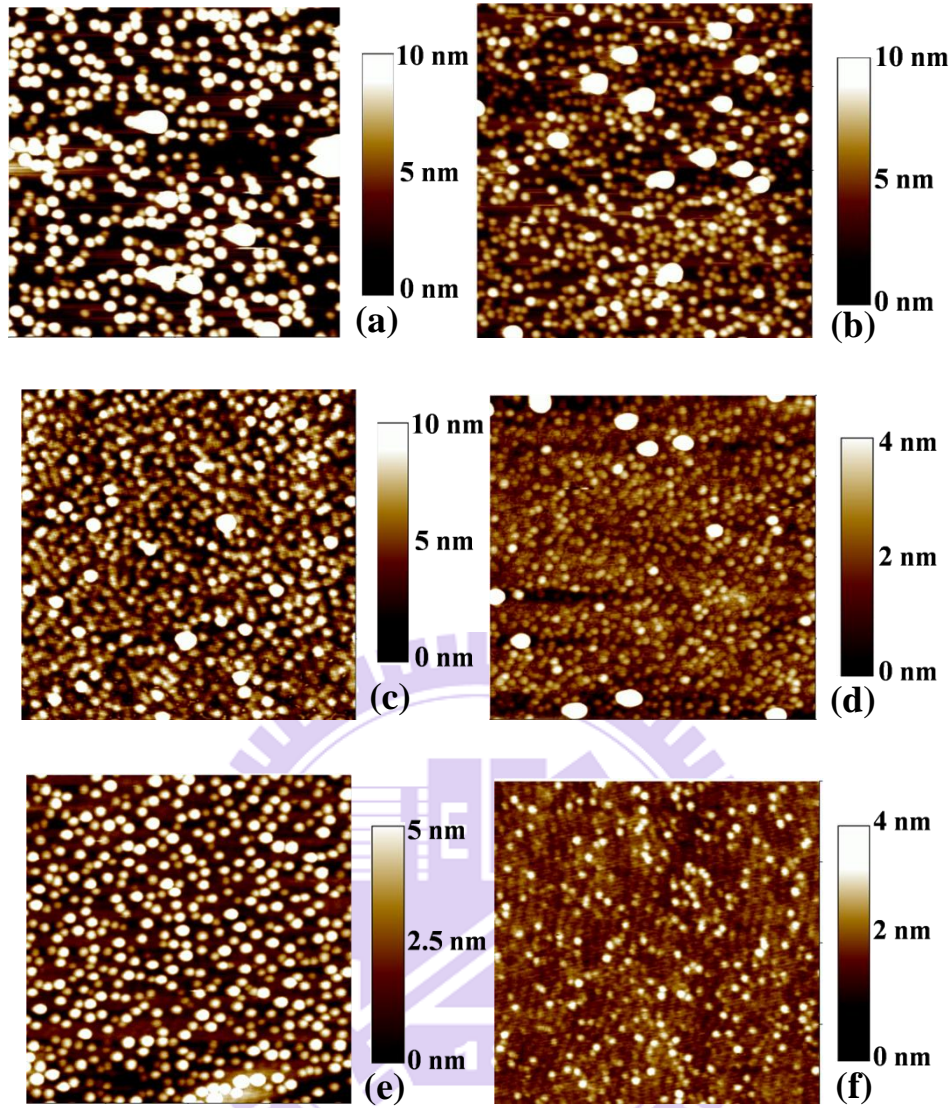


Figure 2-12: AFM images of samples. (a) A (LM4682), (b) B (LM4681), (c) C (LM3572), (d) D (LM3573), (e) E (LM3472) and (f) F (LM4596).

Sample #	T_{growth} ($^{\circ}\text{C}$)	MLs	D ($10^{10}/\text{cm}^2$)	Width (nm)	Height (nm)
A (LM4682)	500	3.0	6.0	54.6	8.3
B (LM4681)	500	2.4	6.8	54.5	5.1
C (LM3572)	480	2.4	8.2	62.4	2.8
D (LM3573)	480	2.4	13	70.4	2.2
E (LM3472)	480	2.6	4.5	39	4.2
F (LM4596)	480	2.0	2.8	31.2	1.9

Table 2-1: Information of the InAs QDs samples. Notice that the substrate of Sample F was not rotated during growth, causing the low density of the portion we use.

Chapter 3

Experimental Observation

In this chapter, we begin to introduce the results of our experimental work: the steady-state and time-resolved spectra of InAs/GaAs QDs. For time-resolved spectra, although there are totally six samples studied, the discussion will be firstly focused on two of them (sample A and C) for clear comparison. We present the first observation of an anomalous spike in the temperature-dependent TRPL around 45 – 85 K, and the spike is shown to be considerably suppressed by high excitation power. Furthermore, several InAs QDs samples with different sizes are studied, and we find that the spike will only occur in the QDs with a particular range of luminance energies.

3.1 Basic Determinations

Steady-state PL spectra

Fig. 3-1 shows the normalized SSPL spectra of the six samples measured at $T = 25$ K under the excitation of a 780-nm laser, with their full-width-at-half-maximum (FWHM) and ground state emission peaks ranging from 1.08 to 1.30 eV, listed in Table 3-1; the non-delta like emission energy is caused by the size-nonuniformity of the ensemble QDs, but in average, we can tell that the size is the largest for Sample A and the smallest for Sample F. In addition, although their FWHM are different among the six samples, we will show that it is irrelevant to the observation.

The steady-state PL is also a necessary work for the determination of detection points for the following TRPL measurement; each TRPL spectrum is detected under a particular PL energy, and unless specially mentioned, the detection points which we aimed at are the energies corresponding to the intensity peak in the SSPL spectra.

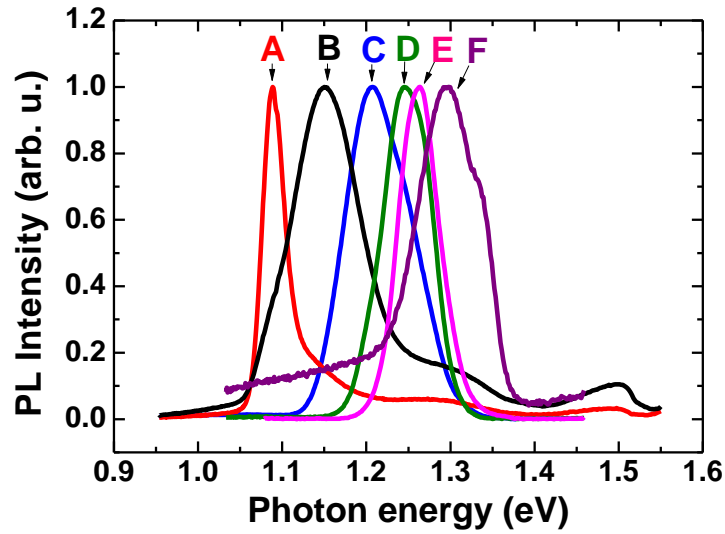


Figure 3-1: SSPL spectra @ T = 25 K of the six samples.

Sample #	A (LM4682)	B (LM4681)	C (LM3572)	D (LM3573)	E (LM3472)	F (LM4596)
Energy (eV)	1.08	1.15	1.20	1.25	1.27	1.30
FWHM (meV)	33	96	90	69	56	98

Table 3-1: List of peak energies and FWHM of the six samples studied in this work.

Steady-state PLE spectra (selective samples)

In addition to SSPL, the SSPL measurements on four selective samples (sample A, C, D, and E) are done at T = 77 K (liquid nitrogen) using a Ti-sapphire laser shown in Fig. 3-2. The horizontal axis of the figure represents the energy difference between the energy of laser (E_{exc}) and a fixed detection PL (E_{det}); the detection PL points are chosen to be the ones corresponding to the (ground state) peak intensities of SSPL spectra at 77 K, and for a particular data point, it means the response of the state higher than ground state with spacing $E_{exc} - E_{det}$. The result shows an analogy for all samples at higher energies; take sample A as an instance: the three peaks at 334, 390 and 427 meV are the response of states of heavy hole, light hole and GaAs,

respectively, which the other three samples also show the similar behaviors at higher energies.

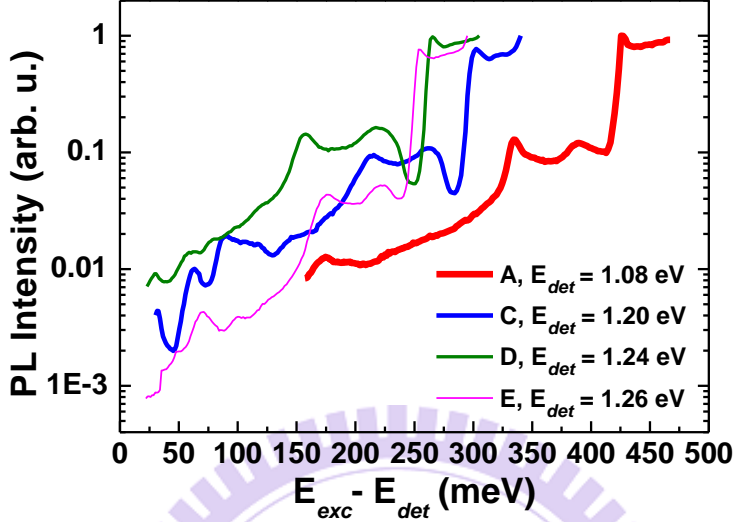


Figure 3-2: SSPLE spectra @ T = 77 K of the four selective samples.

Calculation of numbers of injected electron-hole pairs

The excitation power in the TRPL measurement actually correlates the numbers of injected electron-hole (e-h) pairs per QD per laser pulse, calculated by the following formula:

$$N_{avg} = \frac{P}{R \times E_{laser} \times s} \times (1-r) \times [\exp(-\alpha \cdot x_s) - \exp(-\alpha \cdot x_e)], \quad (3-1)$$

where N_{avg} is the average numbers of injected electron-hole (e-h) pairs per QD per laser pulse; P is the average input power; R is the repetition rate; E_{laser} is the photon energy of the laser; s means the area of the laser spot; r is the light reflection percentage at the sample surface; α is the absorption coefficient of GaAs at 780 nm. Referring to Fig. 2-11 for the structure of the sample, only the two 150nm-GaAs layers adjacent to the embedded QDs will contribute the injected e-h pairs into QDs; if defining the zero point at the top site of the sample, x_s and x_e are respectively the

starting and ending points of these GaAs layers; notice that the $\text{Al}_{0.35}\text{Ga}_{0.65}\text{As}$ layers do not respond to the excitation so their thicknesses are neglected. Moreover, by covering metal except several windows of different sizes (order of μm) left opened on the sample surface, the spot size of the laser can be estimated by adjusting the spot into different windows and checking the intensity of the PL signal. As a result, the spot size is estimated to be roughly $60 \mu\text{m}$ in diameter. For the other parameters, we list them in Table 3-2 with the calculated result under $P = 25 \mu\text{W}$ for sample A (with QD density = $6.0 \times 10^{10} \text{ cm}^{-2}$) as an example.

P (μW)	R (Hz)	E_{laser} (eV)	s (μm^2)	r (%)	α (cm^{-1})	x_s (nm)	x_e (nm)	N_{avg}
25	10^7	1.59	2827.4	30	1.4×10^4	50	150	1.13

Table 3-2: List of parameters used for the calculation of injected e-h pairs.

A Typical result of Temperature-Dependent TRPL of InAs QDs

Being able to fabricate InAs QDs on GaAs matrix in the 1990s [38, 39], the temperature-dependent (T-dependent) TRPL has been widely studied and come up with certain widely-accepted conclusions on both experimental observation and theoretical understanding.

Fig. 3-3 (a) shows the result of T-dependent TRPL of sample A under the excitation of $25 \mu\text{W}$ (average power), demonstrating a typical and well-known result. At low temperature (25-75 K), excitons are “frozen” to have no other special behaviors and the carrier lifetimes in this case are equal to the radiative lifetime, nearly unchanged to be about 0.85 ns. As temperature is raised higher enough to provide carriers with thermal energy to escape from one QD and then recaptured by others in a time comparable with (or even shorter) to the recombination time, the

thermal equilibrium gradually builds up among dot ensembles, known as the effect of “carrier redistribution” [23, 25-27]. As a result, the carrier lifetime increases accompanied by the decrease of FWHM of PL spectra, and the two are clearly observed in our case from 85 to 180 K in Fig. 3-3 (a) and (b). If the temperature is raised higher to near room temperature, the non-radiative recombination becomes dominating [22-24] and consequently cause the carrier lifetimes to decline with a severe drop in integrated PL intensity.

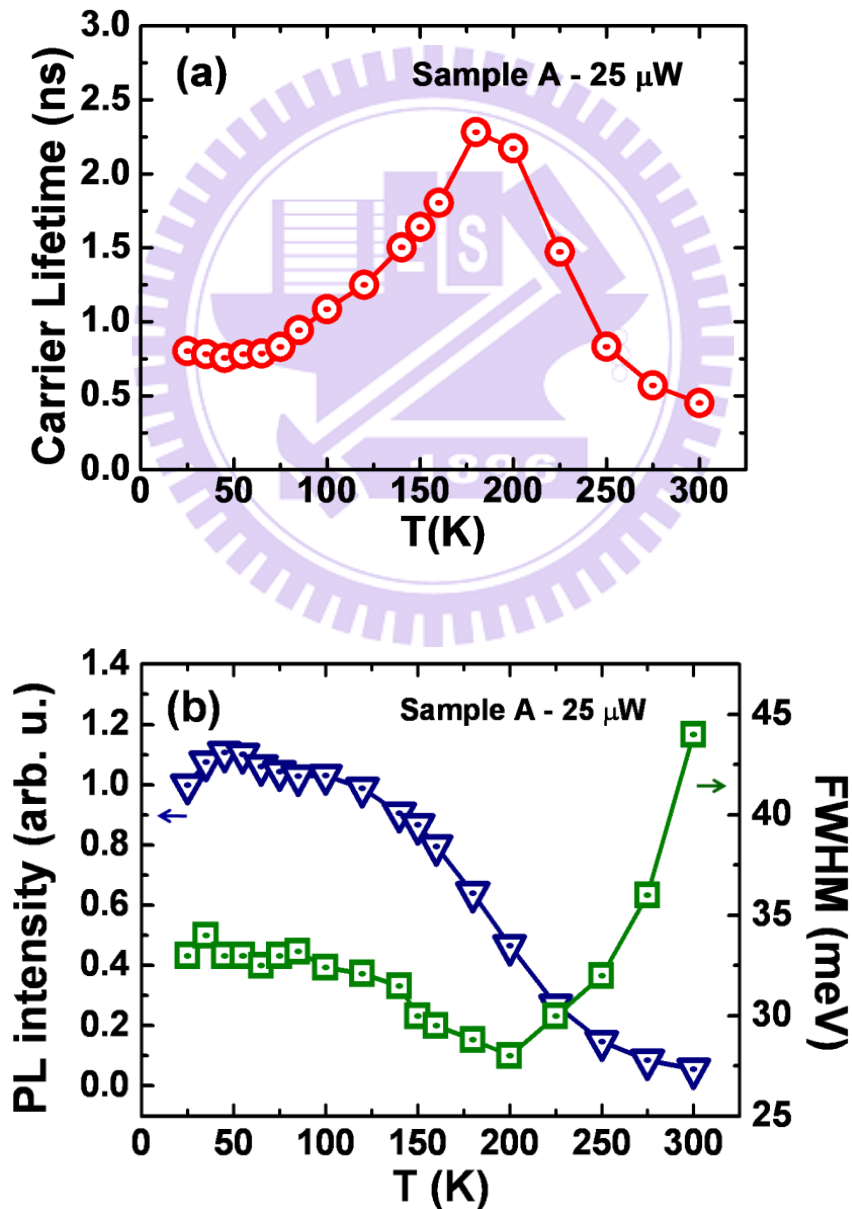


Figure 3-3: (a) Carrier lifetime (τ_1) and (b) PL intensity and FWHM of sample A.

3.2 Low-Temperature Spike of Carrier Lifetimes

3.2.1 Observation and comparison

Compared to the well-known TRPL result for sample A, a surprising result is found in sample C, where an abnormal spike is clearly observed in the range of 50 to 75 K, plotted in Fig. 3-4 (a). In contrast to Sample A, the carrier lifetime of Sample C at 45-85 K behaves a totally distinct way, where it dramatically increases from 1.1 to 4.1 ns from 45 to 60 K, and then decreases back to 2.5 ns at 85 K, showing a spike-like shape; it is worth mentioning that this feature occurs in such a small range which reveals its critical sensitivity to environmental temperature.

At first glance the uncommon phenomenon, one may suspect that the sharp increase and decrease of carrier lifetimes are respectively the deserved consequences of carrier redistribution effect and non-radiative process. None the less, from the PL intensity and FWHM data plotted in Fig. 3-4 (b), we can tell that the physical origins of them are quite different. Firstly, the FWHMs of both samples come to a minimum in the middle temperature range, showing the redistribution effect of thermalized carriers and is responsible for the rise of lifetime in this regime. In addition, the PL intensity decays all the way up to room temperature for both samples due to the growing non-radiative recombination, accompanied with the falling carrier lifetimes. However, in the temperature range which the spike occurs, the trends of both PL intensity and FWHM for the two samples are nearly the same despite their entirely different behavior of carrier lifetimes. Accordingly, we can conclude that the abnormal spike is not resulted from the two well-known mechanisms.

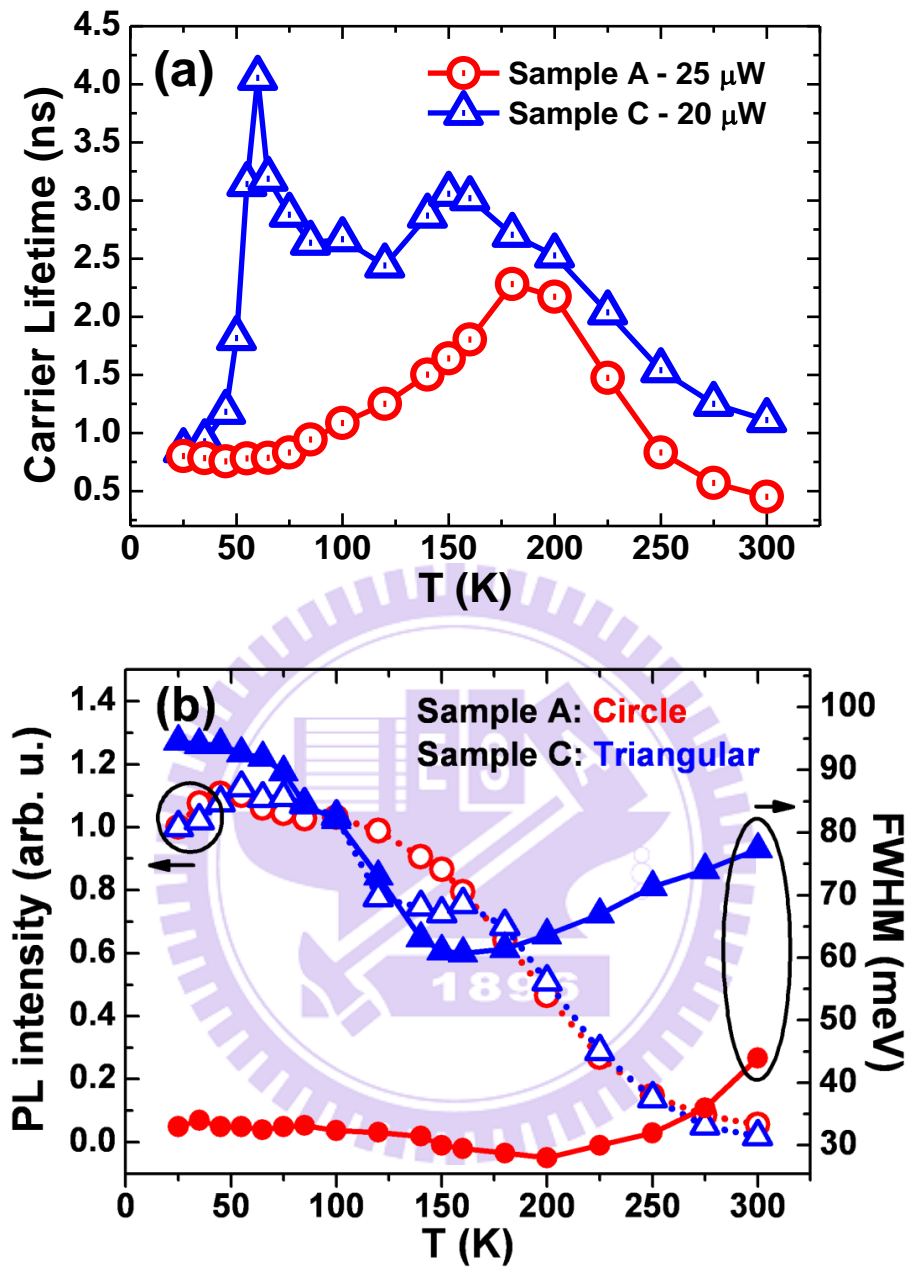


Figure 3-4: (a) Observation of low-T spike phenomenon in sample C; a typical result is shown in Sample A for comparison. (b) Corresponding integrated PL intensity and FWHM for both two samples.

3.2.2 Energy-dependent TRPL

The energy-dependent TRPL of the two samples also studied and the results are plotted in Fig. 3-5 (a) and (b). Except for the peak value of ground state, the TRPL measurements are done under two additional energies, one is higher (represents smaller QDs) and the other is lower (represents larger QDs); we find that for both two samples at the middle temperature range, the carrier lifetimes of different QDs' sizes show a distinction where lifetime of the smaller QDs becomes faster than the larger ones. This can be again attributed to the carrier redistribution effect but from another aspect: the thermalized carriers will escape from smaller QDs and then be recaptured by the larger ones with lower quantized energies; effectively speaking, more portions of total carriers enter the larger QDs, followed by the longer carrier lifetimes. Furthermore, the temperature which the effect begins to reveal is a little higher for Sample A, due to the need of more thermal energy for carriers at lower quantum states to escape from QDs.

In contrast, the carrier lifetimes in the spike regime of sample C are almost quantitatively the same for different detection energies, being another striking evidence for an individual type of its responsible mechanism.

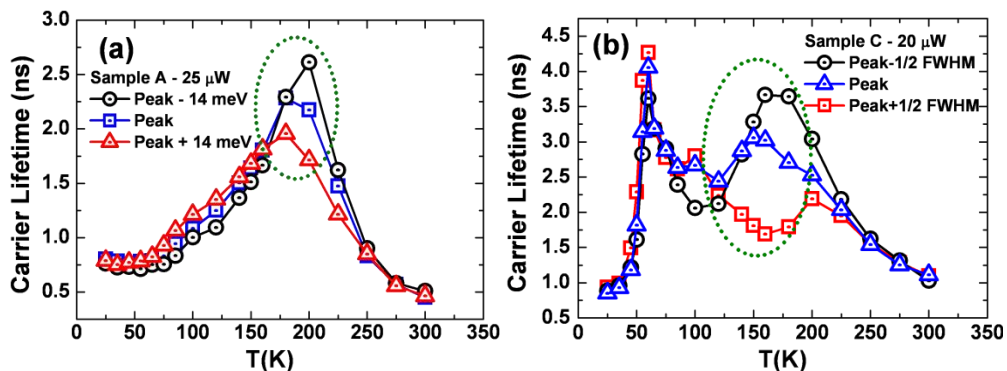


Figure 3-5: Energy-dependent TRPL of (a) Sample A and (b) Sample C. We believe that carrier redistribution occurs in the temperature range circled by dot lines.

3.2.3 Power-dependent TRPL

To further investigate the mechanism of the low-T spike, we have performed power-dependent TRPL measurement of sample C as shown in Fig. 3-6. It is clearly observed that the spike in 45 – 85 K becomes much more obvious under lower excitation and will be considerably suppressed by high power injection; at the lowest excitation power in our measurement ($2 \mu\text{W}$, corresponding to about 0.07 electron-hole pair per QD per pulse by the calculation of Eq. 3-1), the peak lifetime is as high as 7.6 ns. This feature illustrates that the related mechanism of the low-T spike concerns the carrier numbers in QDs.

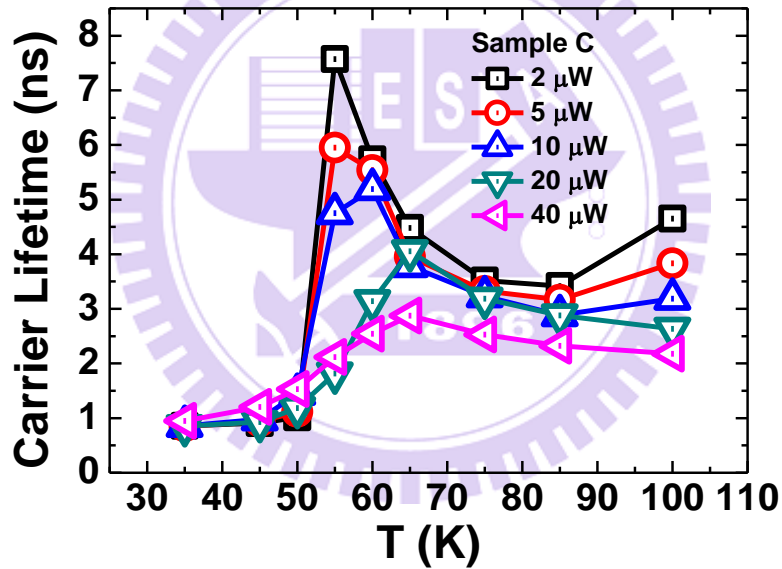


Figure 3-6: Power-dependent TRPL of Sample C.

3.2.4 Decay curves of PL intensity

The carrier lifetimes are the numerical results extracted by mathematical fitting. For a more fundamental perspective, let us now focus on the decay curves directly obtained from the time-resolved measurement under low power excitation, plotted in Fig. 3-7 (a) and (b) for sample A and C, respectively. Note that the PL intensity is in logarithmic scale so the slope of the curve is directly proportional to the inverse of carrier lifetime; the dash lines in the figures just indicate the two exponential components (see Eq. 2-1) of the curves, where the line with light (dark) color represents τ_1 (τ_2). For Sample A, the slopes of both faster and slower part of the decay curves are almost unchanged from 35 to 100 Kelvin, correctly reflecting the fixed lifetimes in Fig. 3-4 (a). Yet, things are absolutely different when it comes to the other sample. For sample C, one can inspect that the faster part of the decay curve is being gradually substituted by the slower as temperature is raised from 35 to 50 K, and finally at $T = 55$ K, the slower part obtains absolute predominance and causes the faster part to totally disappear which makes the original τ_2 now becomes the new τ_1 . Mathematically speaking, the lifetime evaluated as $T = 55$ K is, however, no longer the faster τ_1 but the slower τ_2 , resulting a radical increase in carrier lifetime. In other words, the low-temperature spike occurs at the very temperature which the slower part in the decay curve completely replaces the faster, which is 55 K ($T_{spike} = 55$ K), and the it actually contains the information of both τ_1 and τ_2 regardless the lifetimes reveal just the faster component in each time trace. Furthermore, as temperature rises higher than 55 K, the carrier lifetimes begin to gradually decrease till 75 K and finally re-increases at 85 K.

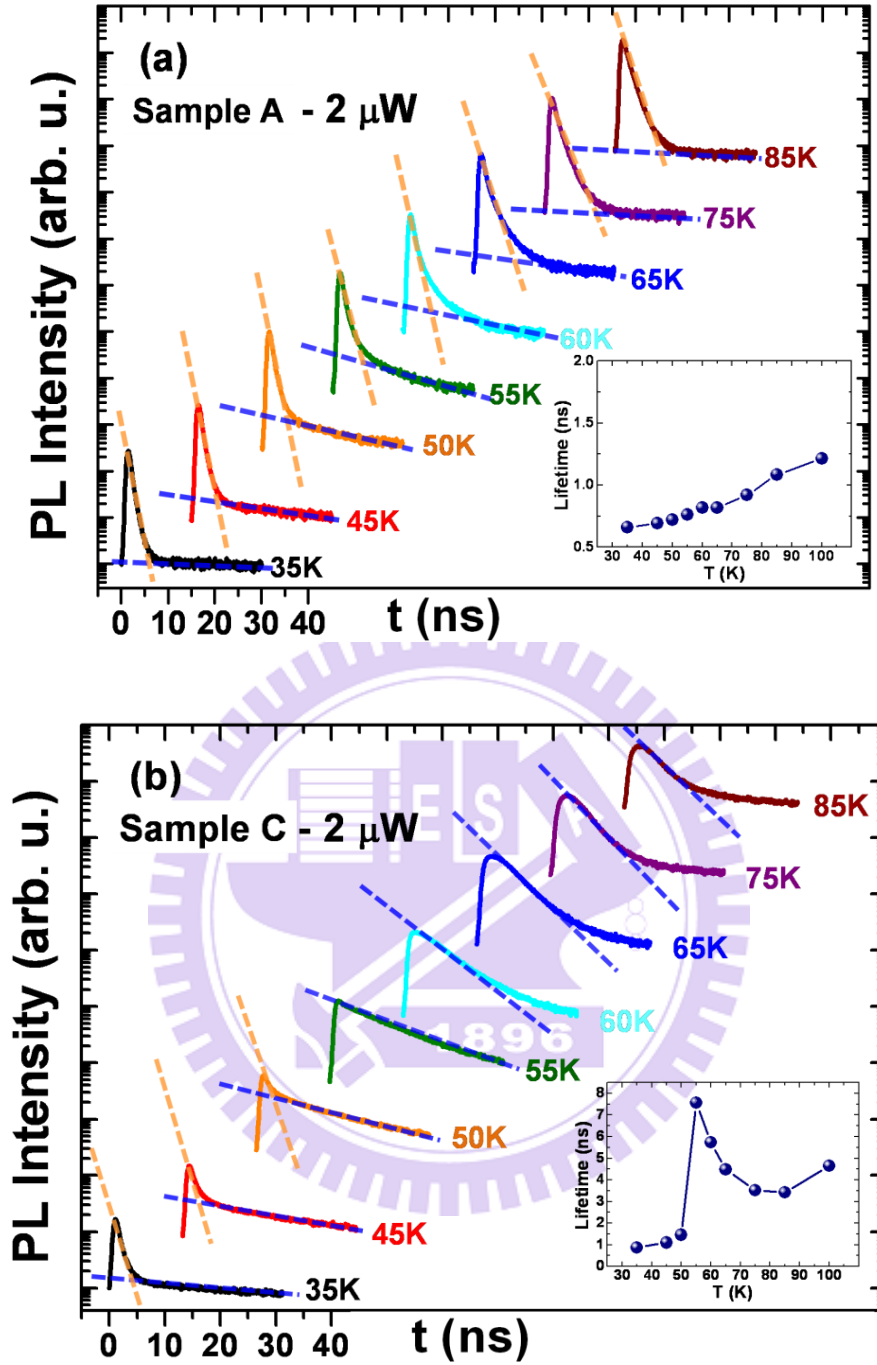


Figure 3-7: Measured decay curves under excitation power of $2 \mu\text{W}$ for (a) Sample A and (b) Sample C with their corresponding τ_1 in the inset figures.

The detailed numerical fitting of these decay curves using Eq. 2-1 also reveals the transition. Based on the fitting parameters in the equation, Fig. 3-8 (a) and (b)

respectively show the τ_1 and τ_2 for Sample A and C, and the ratio of $A_2/(A_1+A_2)$ (named as “ A_2 ratio”) is shown in Fig. 3-8 (c); in this way, we can have a more fundamental view on the behavior of the two part of the decay curves. For Sample C, we find that at $T = 55$ K, the two lifetimes are so close ($\tau_2/\tau_1 < 2$) that the curve can somewhat be treated as a mono-exponential decay function; moreover, its A_2 ratio increases to a maximum of 0.42 at this temperature and then suddenly drop to an order below afterwards which shows that the curves for $T = 60 - 100$ K indeed behave as mono-exponential decay functions, too.

Comparatively for Sample A, its A_2 component remains to be neglectable values while τ_2 still decreases with the rising temperature to 75 Kelvin. Moreover, its A_2 ratio somehow increases from 60 to 75 K (A_2 ratio = 0.16), and τ_2 decreases to the value closet to τ_1 as well at this temperature. Based on all the observations mentioned, it is fair to argue that the phenomenon exists both in the two samples but somehow the *increment degree* of A_2 ratio is large enough to reveal it more clearly.

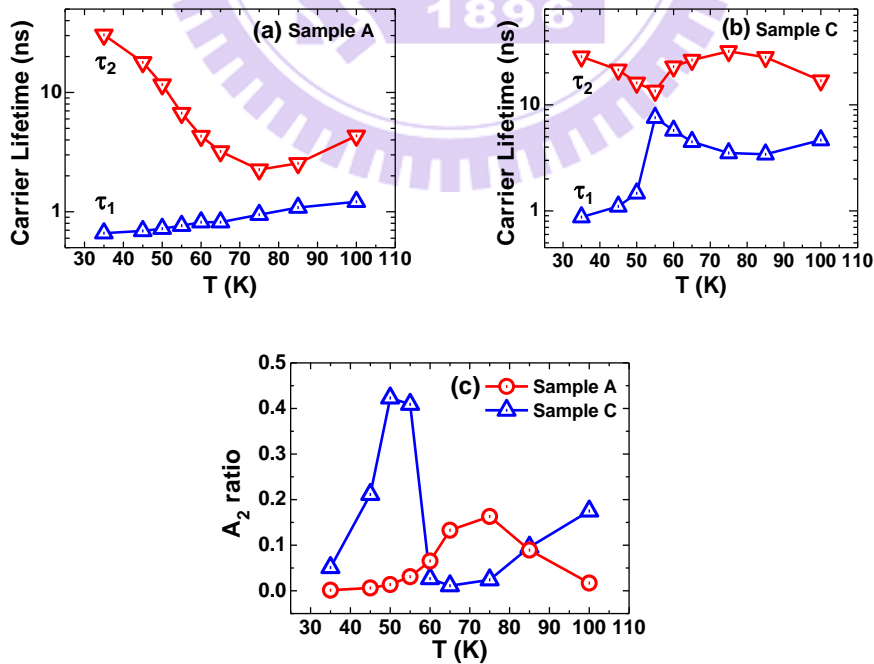


Figure 3-8: Parameters evaluated from numerical fitting for (a) Sample A and (b) Sample C; (c): comparison of A_2 ratio of sample A and C.

3.3 The Prolonged Rising Time

As mentioned previously that the time resolution of our system is too low to measure the picosecond-order carrier relaxation; in other words, the rising time of the photon intensity will be approximately the value of our system resolution. Nevertheless, we show in Fig. 3-9 (a) and (b) that for Sample C, the rising time is qualitatively prolonged to the degree detectable for the system (~ 1 ns) as temperature rises whereas no such phenomenon is observed in Sample A.

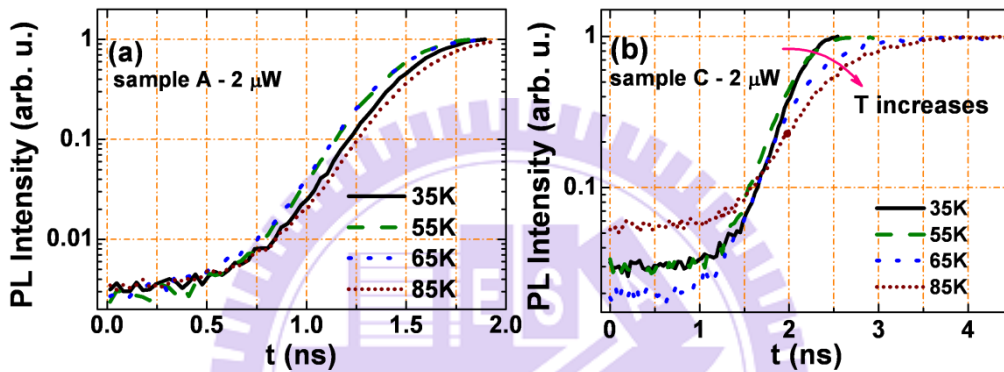


Figure 3-9: Rising parts (measured in our system) of (a) Sample A and (b) Sample C.

3.4 Size Dependence of QDs on the Low-T Spike

The previous comparison of TRPL results are focused on the two samples and the spike somehow occurs only in the one with higher quantized energy. To check whether this phenomenon is dependent on the sizes of QDs, we bring the other four samples into study.

Fig. 3-10 shows the T-dependent carrier lifetimes of all the six samples under the excitation of 10 μ W (due to experimental limitation, the lowest excitation power measured for Sample F is 10 μ W; however, the power is low enough for qualitatively observation in all samples). We discover a surprising result that within this wide range of ground states energy from 1.08 to 1.30 eV, only those QDs with intermediate sizes

will reveal the spike-like feature. Moreover, although the spike are shown only in the three samples with intermediate ground state energies: Sample C (1.20 eV), Sample D (1.25 eV), and Sample E (1.27 eV), the peak values of carrier lifetimes among them remain an obvious difference, being the highest for Sample D.

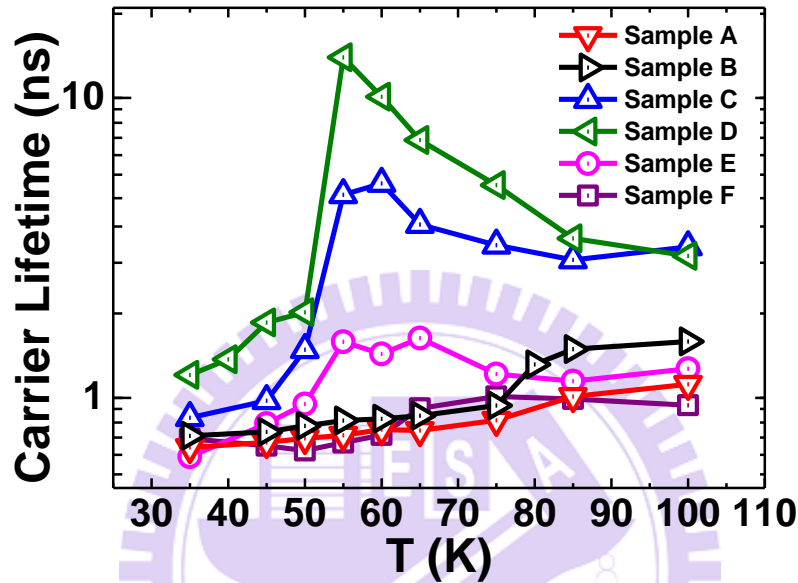


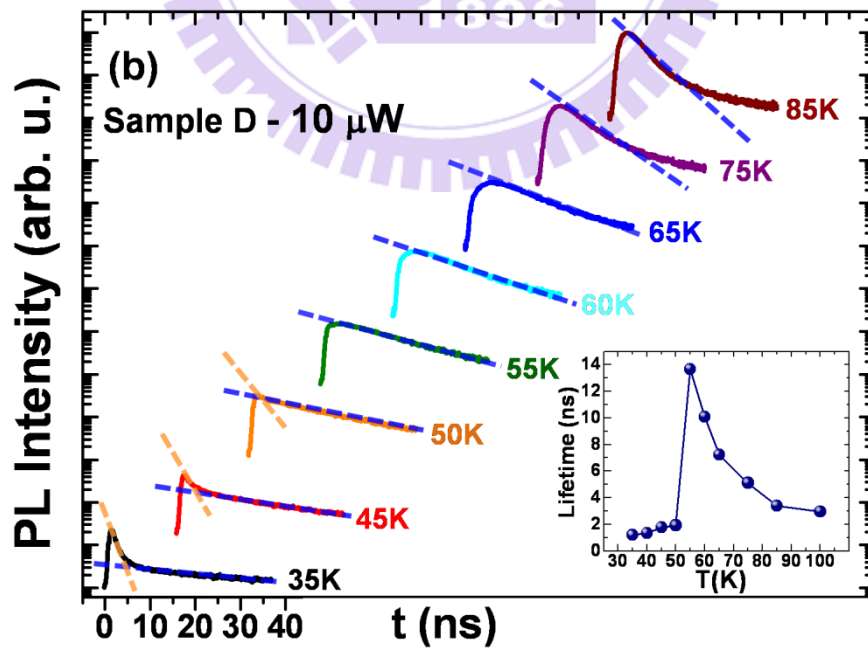
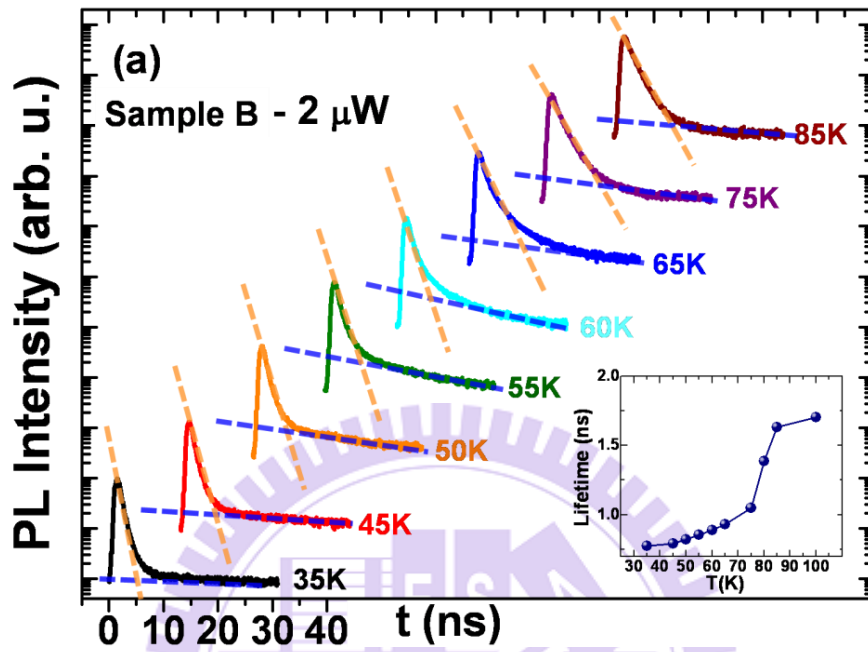
Figure 3-10: T-dependent carrier lifetimes (τ_1) for all six samples under $10 \mu\text{W}$.

In addition, except the two previously discussed, the decay curves under the lowest excitation of the other four samples are shown in Fig. 3-11 (a) to (d) with their corresponding carrier lifetimes,* and the fitting parameters for each of them are shown in Fig. 3-12 (a) to (e) to meet the completeness of the whole study.

A similar trend is observed that τ_2 decreases as temperature rises. However, the A_2 component barely has the portion of less than 10 % in the decay curves for all samples except Sample D; for Sample D, A_2 violently increases to the value even larger than A_1 at 50 Kelvin and immediately quenches to approximately zero, which behaves very similarly as the case in Sample C. This rather clear comparison again

*For the measurements below $10 \mu\text{W}$ of sample D, the carrier lifetimes are not extractable because the decay curves cannot be numerically well fitted. We show the case of $10 \mu\text{W}$ without loss of generality.

demonstrates that the phenomenon may be universal but it is the increment degree of A_2 ratio which matters (sample C and D).



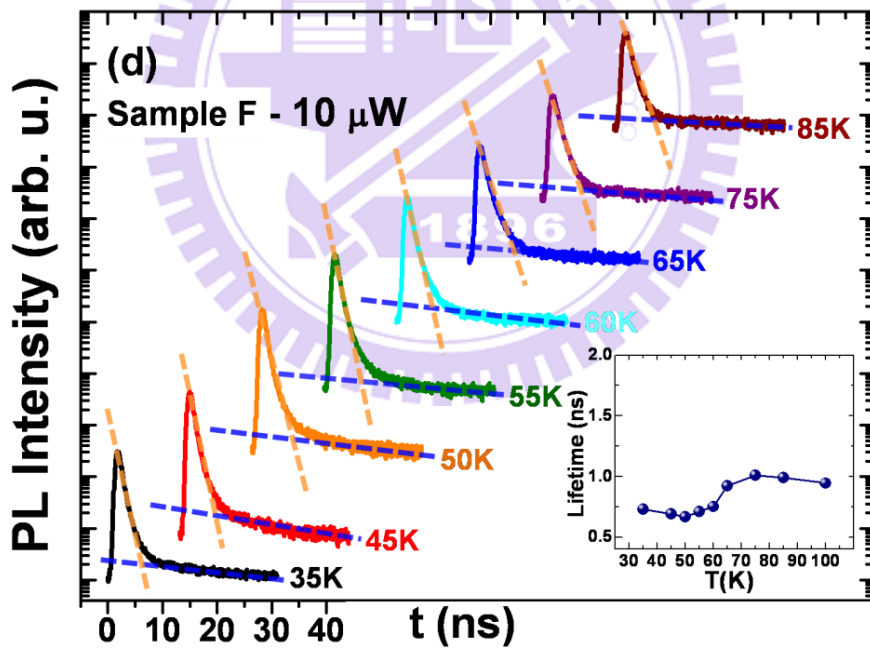
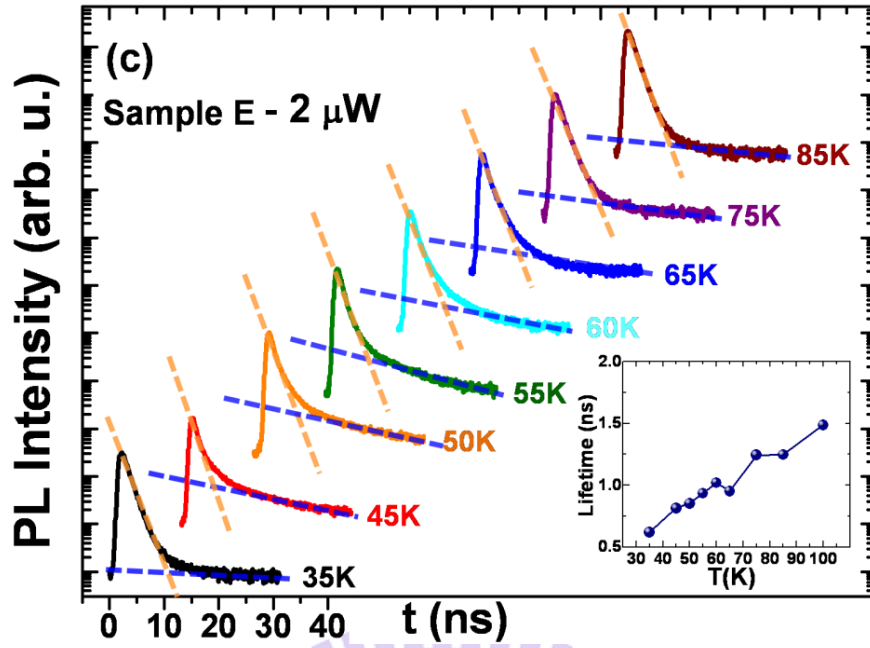


Figure 3-11: Measured decay curves of (a) Sample B, (b) Sample D, (c) Sample E and (d) Sample F with their corresponding τ_1 in the inset figures.

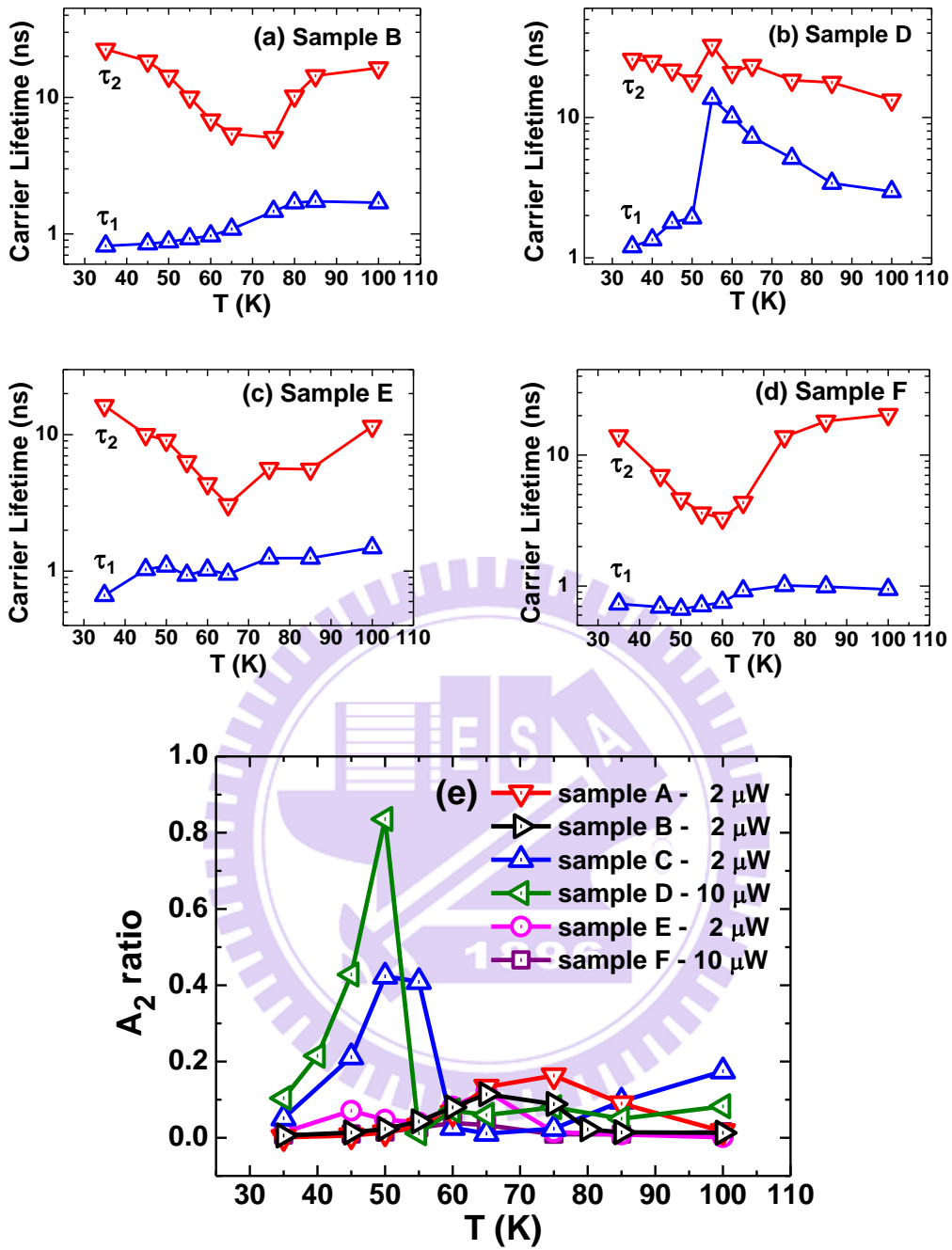


Figure 3-12: Fitting parameters of all six samples. (a) to (d): τ_1 , τ_2 of sample B, D, E and F, respectively; (e): A₂ ratio of all six samples.

3.5 Issues about the Sizes of QDs

Although the size dependence of the low-T spike is demonstrated in the last section, things are more complicated than we think. The steady-state PL spectra (Fig. 3-1) show that there exists an overlapping range for Sample C and B; according to the size-dependent argument mentioned in section 3.4, one may predict to observe the low-T spike if measuring TRPL under similar detection wavelength, regardless which sample we choose. Unexpectedly, this is not the case; referring to Fig. 3-13 (a) and (b), we find that in spite of the close detection energies (ϵ_1 , ϵ_2 and ϵ_3 equal to respectively 1.15, 1.20 and 1.16 eV) of the two samples, the spike is only observed in Sample C (ϵ_3).

The “sample-dependent” observation indicates that the conditions for the spike to occur are not merely the size of QDs and excitation power but also other factors; the complexity of these factors may play a critical role, for instance, the distribution of strain for different QDs’ shapes or the dependence of intrinsic relaxation on energy spacing. However, these extra considerations are not discussed in this work.

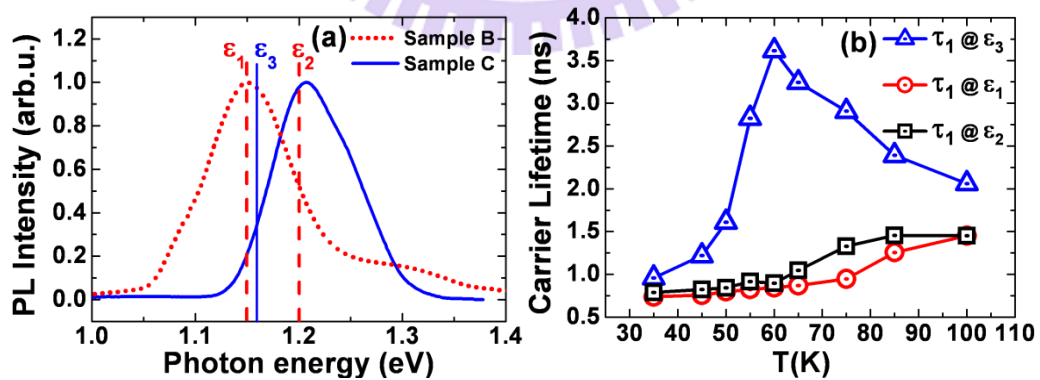


Figure 3-13: (a) SSPL spectra for sample B and C. The detection energies of TRPL are ϵ_1 , ϵ_2 for sample B and ϵ_3 for sample C; (b) corresponding τ_1 at different temperatures.

Chapter 4

Simulation and Comprehension

To establish a comprehensive picture of the experimental observation, we propose a theoretical model involving three excitonic states in our simulation work. The model is solved numerically in rate equations and the output decay curves are then fitted by exactly Eq. 2-1 to evaluate τ_1 and τ_2 to be the faster and slower carrier lifetimes, respectively. In addition to the simulation result, most importantly, the related physical significances are investigated, which analyzes the capability and limitation of this model to clarify the perspectives in future works.

4.1 Dark, Bright and Hot States (Excitons)

For InAs QDs, the confinement provided by the system is fine enough for both electrons and holes, so it is reliable to treat them together as excitons. The model used for simulation involves three quantized excitonic states in QDs: the dark, bright and hot states. They are shown in Fig. 4-1 and we now introduce the physical pictures for each of them.

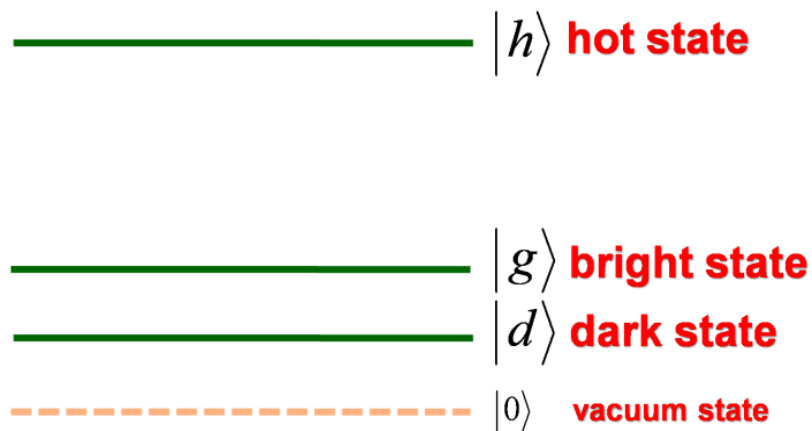


Figure 4-1: Three excitonic states in our model. The “vacuum” level merely means the states of QDs without any excitons.

The dark and bright states are actually closely related. Fig. 4-2 schematically shows the main difference between the two; the degeneracy of the ground state is split due to the exchange coupling between the spins of electron and hole for bright excitons, which let dark excitons attain the total angular momentum to be $\pm 2\hbar$ while for bright excitons the value is $\pm \hbar$; the energy splitting between the two (Δ_{gd}) is typically few hundreds of μeV with the bright level above [40]. However, recombination is only allowed for bright excitons because of the restriction of selection rule, and for the other that cannot recombine, excitons are optically inactive, or “dark”. As for the hot state, it is formed by either the electron or hole at its ground state and the other at its first excited level.

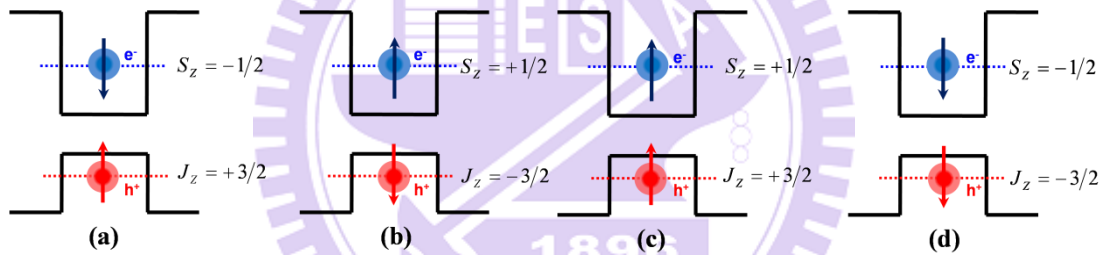


Figure 4-2: Spin alignments of excitons; total spin angular momentum = (a) $-\hbar$, (b) \hbar , (c) $2\hbar$ and (d) $-2\hbar$; (a) and (b) are bright excitons while (c) and (d) are dark excitons.

A Short Review on the Spin-Flip Relaxation

The spin dynamics in self-assembled QDs has caught great attention not only because the curiosity to further discover the fundamental behavior of QDs but with the expectation on the application of spintronic-based devices. In fact, the relevant mechanisms for spin relaxation in QDs are still being debated; Khaetskii and Nazarov [41] showed that the usually responsible mechanisms for spin dynamics in bulk is

much less effective for sub-levels in QDs. On the other hand, it is argued that the hyperfine effect, or the interaction between electrons and nuclei is the dominant mechanism for the relaxation [42, 43]; the admixture of two independent spinors [41], spin-orbit coupling of holes in V.B. [44], phonon interaction and the mixing of light- and heavy-hole bands [45] are all proposed by theoretical researchers. However, the calculated spin-flip rates attributed to the above mechanisms fail to meet the experimental value, which is much faster [46, 47]. Thrilling, Liao *et al.* [48] recently studied the hole-Dresselhaus spin-orbit coupling and it leads to a result close to the observed values in InAs QDs [46]. As for our case, we now solve that rate equations based on the three-level system and study the spin dynamics theoretically together with the experimental data.

Carrier Transitions in the System

Since we are dealing with the dynamic behaviors of carriers, the state-to-state transition must be considered in detail. In spite of recombination is forbidden at dark state, it is allowed supposing that excitons can relax back to bright state by a spin-flip process mediated by phonons. However, it is reported that the spin-flip time, or $\tau_{spin-flip}$, is fairly long to be about 100 ns at low temperature [46] compared to the usual radiative lifetime (1 ns) for InAs self-assembled QDs.

In contrast to the very slow transition process between the dark and bright state, the relaxation from hot state to either ground or bright states can be pretty fast. In fact, the issue was under debate in a period; some research groups report the existence of “phonon bottleneck” which results a long relaxation time (\sim ns) [49, 50], whereas a great amount of recent works conversely deny the contention and advocate the relaxation time must be in the order of ps [32, 51-55]. Although the observations are

so contradictory, we believe the latter is more likely in our case since the energy spacing in this case is in the order of meV, reasonably making the carrier relaxation much more effective.

4.2 Rate Equations

Rate equations are useful for characterizing the carrier dynamics among various states in a system; with distinct transition rates, the dynamics can be so different. For example, the spin-flip relaxation from dark to bright state will be much slower than the relaxation from hot to bright state, even if the two events equally represent a transition from one level to another. The main goal of solving rate equations is to monitor the carrier variations with respect to time in particular states, which further helps us create correspondence in the existing experiments. For the three-level system referring to the states shown in Fig. 4-1, the mathematical expressions contain three differential equations with each of them coupled with the other two, which are:

$$\begin{aligned}
 \frac{dN_g}{dt} &= - \left[\frac{N_g}{\tau_{rad}} + \frac{N_g}{\tau_{gd}} \left(1 - \frac{N_d}{n_d} \right) + \frac{N_g}{\tau_{gh}} \left(1 - \frac{N_h}{n_h} \right) \right] + \left[G_g(t) + \frac{N_d}{\tau_{dg}} \left(1 - \frac{N_g}{n_g} \right) + \frac{N_h}{\tau_{hg}} \left(1 - \frac{N_g}{n_g} \right) \right], \\
 \frac{dN_d}{dt} &= - \left[\frac{N_d}{\tau_{dg}} \left(1 - \frac{N_g}{n_g} \right) + \frac{N_d}{\tau_{dh}} \left(1 - \frac{N_h}{n_h} \right) \right] + \left[G_d(t) + \frac{N_g}{\tau_{gd}} \left(1 - \frac{N_d}{n_d} \right) + \frac{N_h}{\tau_{hd}} \left(1 - \frac{N_d}{n_d} \right) \right], \\
 \frac{dN_h}{dt} &= - \left[\frac{N_h}{\tau_{hg}} \left(1 - \frac{N_g}{n_g} \right) + \frac{N_h}{\tau_{hd}} \left(1 - \frac{N_d}{n_d} \right) \right] + \left[\frac{N_g}{\tau_{gh}} \left(1 - \frac{N_h}{n_h} \right) + \frac{N_d}{\tau_{dh}} \left(1 - \frac{N_h}{n_h} \right) \right].
 \end{aligned} \tag{4-1}$$

The subscripts “d”, “g”, and “h” respectively represent the dark, ground and hot states. Since we are only interested in the “decaying” behavior instead of the rising, we let the carrier generation be initially at ground and dark state with a Gaussian distribution, $G_i(t)$; as regards the hot state, we assume that all carriers will be captured by the other two states so no generation is given at this level. For N_i , it stands for the number of carriers at the i state; for electrons and holes are fermions, their occupation obeys the Pauli exclusion principle, giving n_i to be the its maximum allowable carriers.

As for the important transition, τ_{rad} is the radiative lifetime of excitons, and for the transition time from a lower to the hot state, we consider the case of thermalized carriers whose distribution follows the Maxwell-Boltzmann statistics:

$$\tau_{d(g)h} = \tau_{hd(g)} \cdot e^{-\Delta_{hd(g)}/k_B T}, \quad (4-2)$$

where k_B is the Boltzmann constant, $\tau_{hd(g)}$ being the transition lifetime from the dark (d) or ground (g) to hot state (h) and vice versa with the energy spacing of the two equals to Δ . For the spin-flip rate, it has been discussed in many papers both experimentally [46] and theoretically [45, 48, 56]; however, due to the very small Δ_{gd} , here we assume the rate to be a constant ($\tau_{gd} = \tau_{dg} = \tau_{spin-flip}$) independent of either Δ_{gd} or temperature for simplicity, and it will be clear that the exact value of $\tau_{spin-flip}$ is unimportant as long as it is large enough. Lastly, non-radiative recombination is not considered according to the SSPL intensity showing a nearly constant value below 100 Kelvin (Fig. 3-4 (b)). After setting the initial parameters, the rate equations are numerically solved using first-order approximation with $dt = 0.1$ ps (Eqs. 4-1). Finally, the decay curves of the bright state are obtained and the carrier lifetimes are then extracted by fitting the curves with Eq.2-1. As a whole, we give a flow chart in Fig. 4-3 to summarize the simulation procedures more clearly.

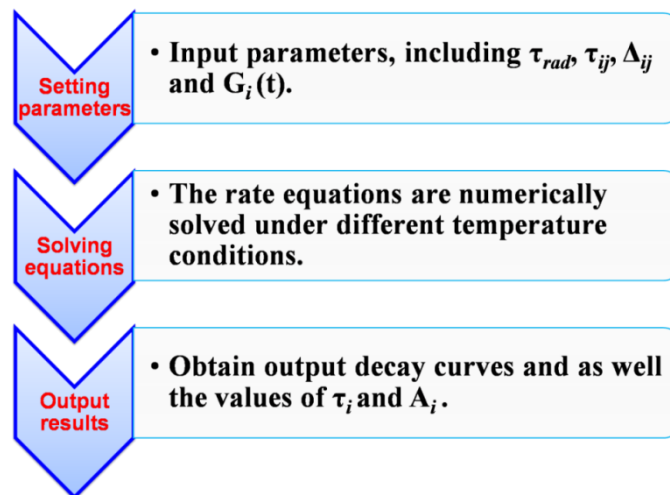


Figure 4-3: Flow chart of the simulation procedures.

4.3 Simulation Results

By setting the values of parameters all with widely-accepted numbers listed in Table. 4-1, we can get the respective results of τ_1 and τ_2 plotted in Fig. 4-4 (a) and (b). The result shows that the simulated τ_1 is quantitatively well-fitted to the experimental data from 35 and 75 Kelvin while slight differences are shown for τ_2 at 45 and 50 Kelvin. Notice that the inconsistency at 85 K of τ_1 is caused by the re-increase of the experimental values. However, referring back to Fig. 3-4 (a) and Fig. 3-5 (b), the carrier redistribution effect starts approximately at this temperature, so we believe it is due to the mechanism not taken into account in our simulation.

In fact, the critical transition from τ_1 to τ_2 can also be obtained in the simulation, as shown in Fig. 4-5 of the decay curves, where one can clearly observe the change from bi-exponential to mono-exponential decay right at $T = 55$ K. On the other hand, the stimulated A_2 ratio increases to as large as 0.64 at 50 Kelvin (Fig. 4-6) and as $T > 55$ K, the decay curve changes into mono-exponential decay, meaning $A_2 = 0$.

Parameter	τ_{rad}	τ_{hd}	τ_{hg}	$\tau_{spin-flip}$	Δ_{hg}	Δ_{gd}
Value	1 ns	10 ps	10 ps	35 ns	28.7 meV	300 μ eV
Parameter	#	n_g	n_d	n_e	G_{gi}	FWHM
Value	0.25	2	2	16	13 %	100 ps

Table 4-1: Parameters used in simulation. #: numbers of excitons per QD per laser pulse; FWHM: FWHM of the Gaussian generation (specification of the pulsed laser: 70 ps). G_{gi} : portion of carriers initially given at the ground state.

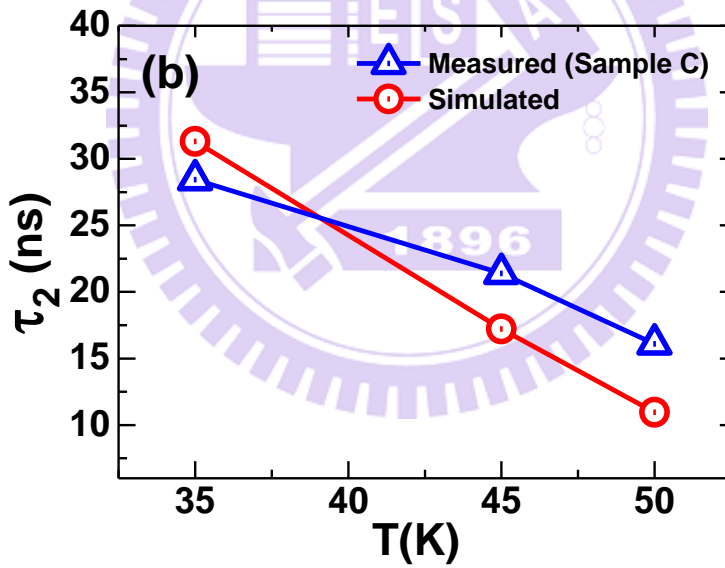
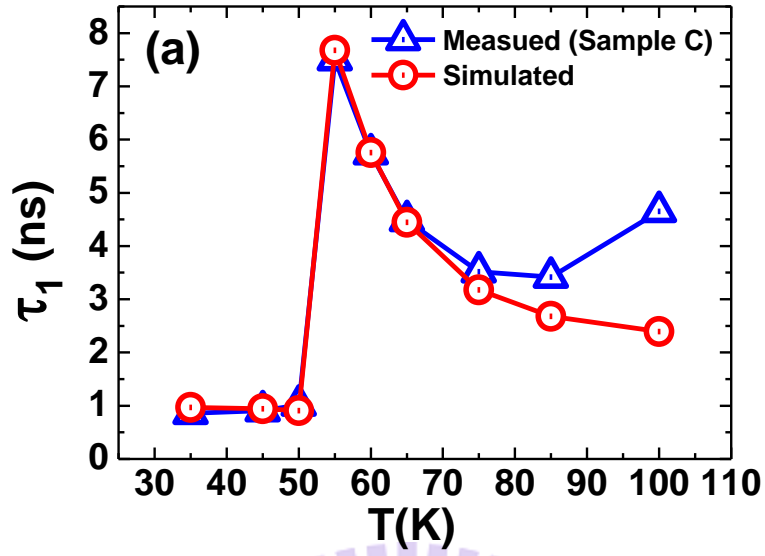


Figure 4-4: Comparison of (a) τ_1 and (b) τ_2 with simulation and experiment. No simulated data points of τ_2 for $T \geq 55$ K because the decay curves become mono-exponential decay.

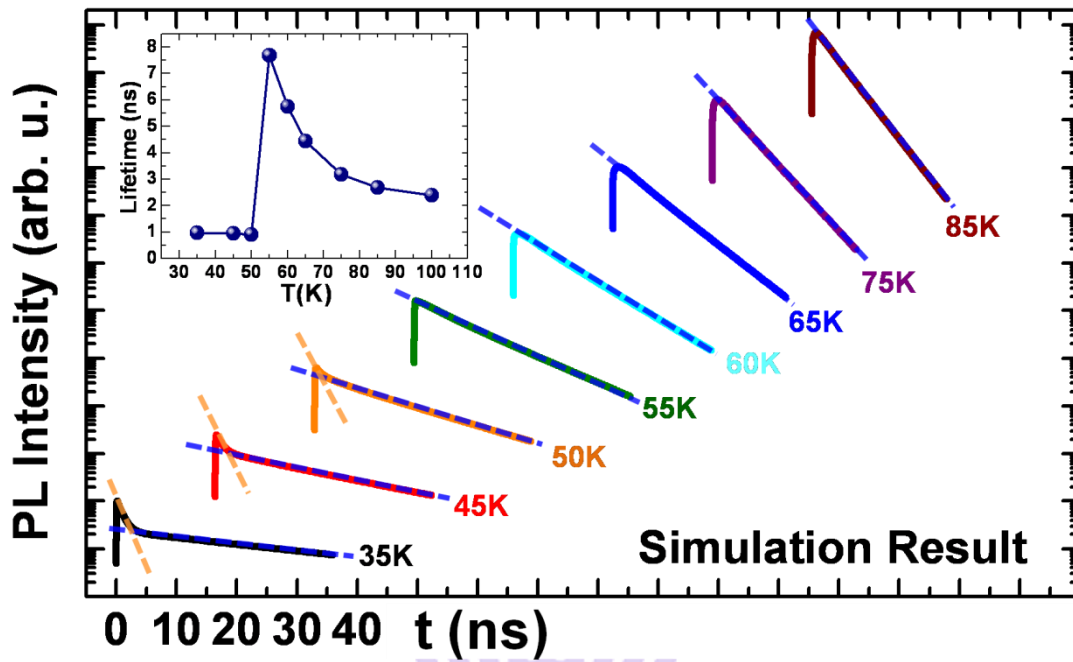


Figure 4-5: Decay curves obtained from simulation. The “transition” of the lifetimes as in the experimental case is clearly shown. Inset: corresponding τ_1 of simulation.

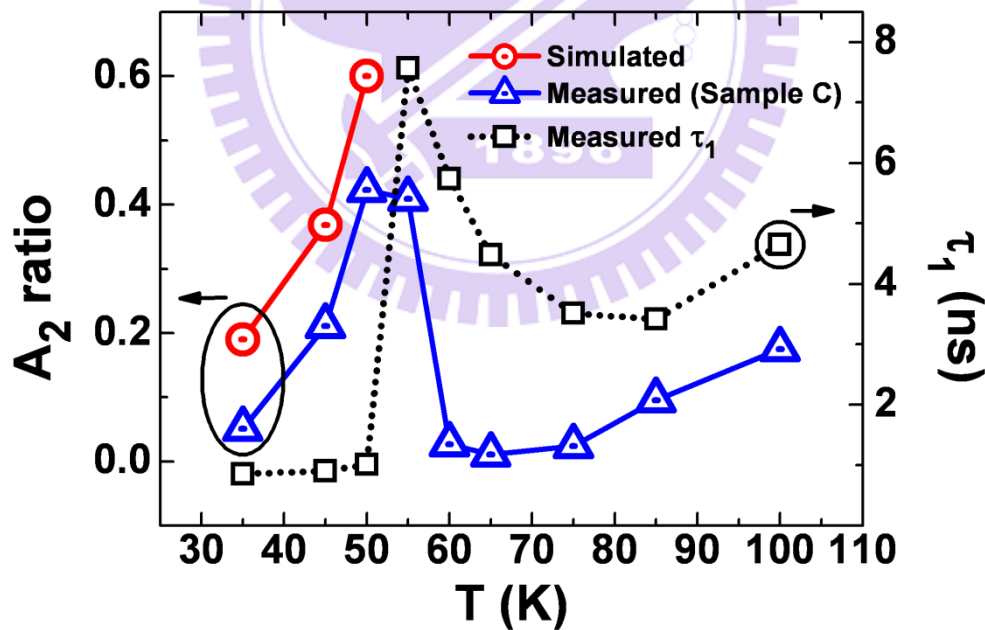


Figure 4-6: A_2 ratio at different temperatures with the corresponding τ_1 . For $T \geq 55$ K, no data point for simulation since the curves become mono-exponential decay.

4.4 Mechanisms – the Effect of Temperature

4.4.1 Main discussion

When it comes to modeling, the fit between the experiment data and theoretical prediction is basically the mathematical acquirement; what really matters is the valuable physical concept obtained from the simulation. It should be emphasized that temperature is the most substantial manipulated variable in this whole study so the following discussion will be centered on its effect.

Considering excitons occupying both dark and bright states at low temperature, for the lack of thermal energy, the only option for depleting dark excitons is to have them relax back to the bright states for recombination through a spin-flip process, whose rate is fairly slow (Fig. 4-7 (a)). In this case, the time-dependent PL intensity (PL time trace) of the bright state will indeed be a bi-exponential decay function where the faster part is due to the recombination of bright excitons while the slower is attributed to the recombination after the spin-flip process for dark excitons.

None the less, things become quite different as temperature rises. As shown in Fig. 4-7 (b), since carriers have enough thermal energy, they can be firstly thermalized to the hot state and then relax back to bright state for recombination; compared to the spin-flip relaxation, this additional path is such a much faster process that carriers prefer, and we believe that the spin angular momentum can be realigned with a larger probability during the process. Consequently, as temperature is raised, carriers are capable to continuously compensate the consumption of the radiative recombination from the additional path, making the decay rate to slow down and the measured τ_1 prolonged significantly.

As for τ_2 , a decrease is observed as temperature rises both in experiment and simulation (Fig. 4-4); this is because carriers are now shared by a faster extra process

favored by thermal energy. Based on the above argument, τ_2 correlates two mechanisms: the slow spin-flip process and the additionally fast relaxation path. Having this concept in mind, the decrease of carrier lifetime after $T = T_{spike}$ now seems to be intelligible as much more dark excitons are able to relax through the additional path instead of being trapped by the spin-flip bottleneck. Besides, we would like to point out that the additional path already exists at low temperature, but the key for it to be activated depends on whether the temperature is high enough or not.

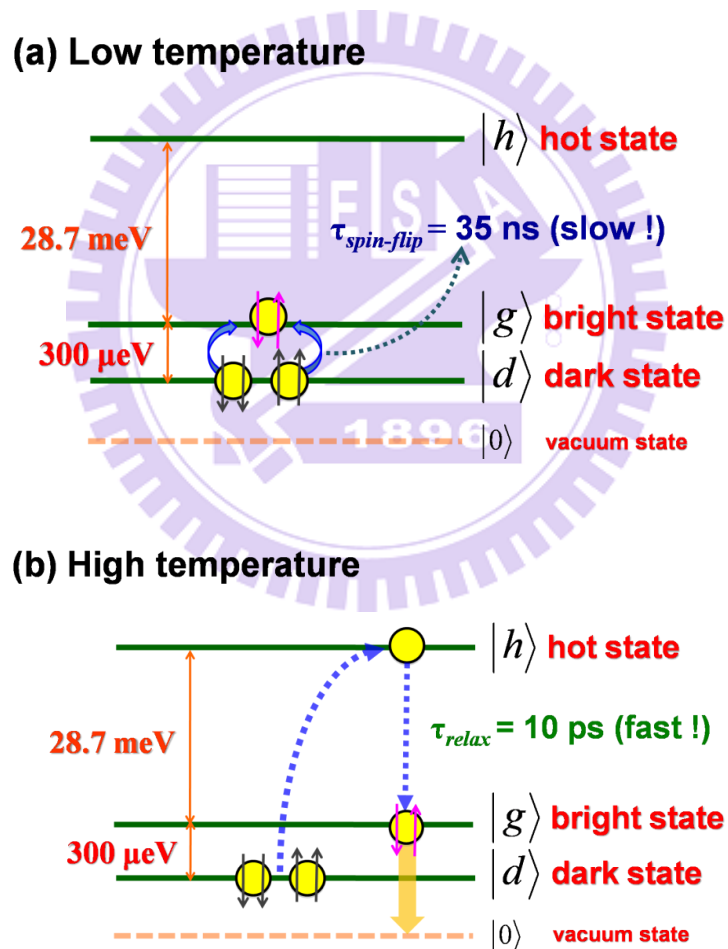


Figure 4-7: Carrier dynamics at low and high temperatures. (a) At low temperature, dark excitons can only relax to bright excitons through the slow spin-flip process. (b) At high temperature, dark excitons can relax through an additional path with a much faster rate.

The additional path – physical picture

One would indeed like to know the central concept to fulfill the eagerness of acquiring the physical values of this model. For a start, we seek for an analytical solution of rate equations by making some (reasonable) simplifications in the original system. Firstly, the spin-flip rate is so slow that we assume τ_{hg} to be infinity (i.e. dark excitons cannot relax to bright excitons through the spin-flip process); second, the Pauli exclusion limitation is not considered since we deal with the case of low excitation power; finally, τ_{gh} is too long at low temperature compared to τ_r (1 ns) so we neglect it as well. Moreover, we introduce a new parameter, τ_{eff} , representing the *effective* transition time for dark excitons to relax to bright states *through the additional path*, which is nothing but:

$$\tau_{eff} = 2 \times \tau_{dh} = 2 \times \tau_{hd} \cdot e^{\Delta_{hd}/k_B T}, \quad (4-3)$$

where the factor “2” comes from the equal chance for dark excitons to relax to either bright or back to dark states ($\tau_{hg} = \tau_{hd} = 10$ ps). In Fig. 4-8, we plot the temperature dependence of τ_{eff} under the conditions of $\tau_{hd} = 10$ ps and $\Delta_{hd} = 28.7$ meV, which shows that τ_{eff} is really long at low temperature but exponentially decreases to the value smaller than 10 ns as temperature rises to 55 K.

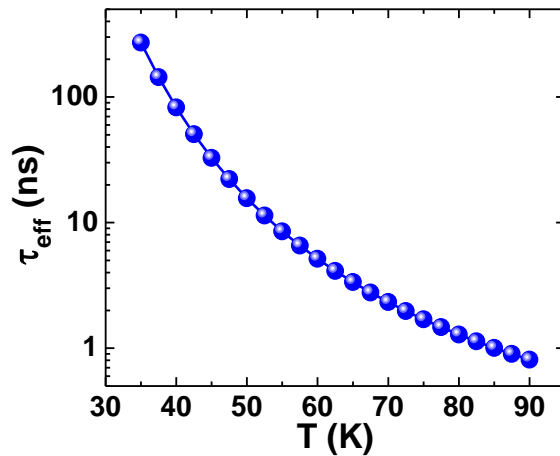


Figure 4-8: τ_{eff} as a function of temperature.

If considering only the relaxation through additional path (τ_{eff}) and the radiative recombination (τ_r) like the system schematically plotted in Fig. 4-9, the corresponding rate equations are:

$$\begin{aligned}\frac{dN_g}{dt} &= -\frac{N_g}{\tau_r} + \frac{N_d}{\tau_{eff}}, \\ \frac{dN_d}{dt} &= -\frac{N_d}{\tau_{eff}}.\end{aligned}\quad (4-4)$$

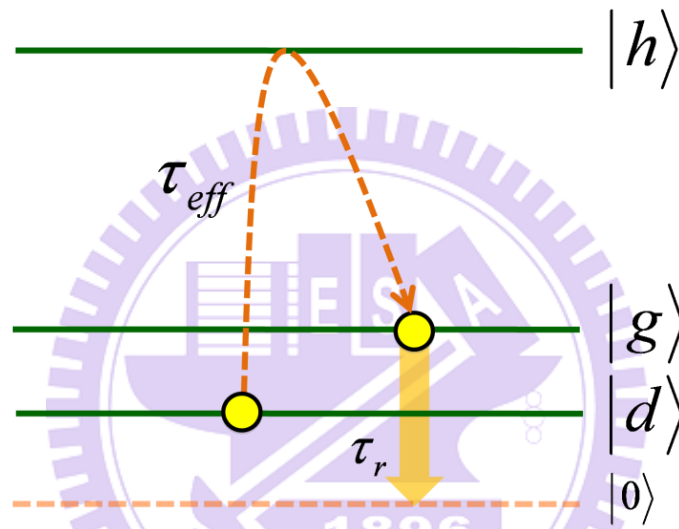


Figure 4-9: Simplified model with the new introduced parameter τ_{eff} .

Note that the terms of hot states are just considered in τ_{eff} so N_h does not appear in Eq. 4-4; the coupled equations can be easily solved to get the decay relation of N_g :

$$N_g(t) = \left(N_{g0} - \frac{N_{d0} \cdot \tau_r}{\tau_{eff} - \tau_r} \right) \exp\left(-t/\tau_r\right) + \frac{N_{d0} \cdot \tau_r}{\tau_{eff} - \tau_r} \exp\left(-t/\tau_{eff}\right), \quad (4-5 (a))$$

$$A_1 = N_{g0} - \frac{N_{d0} \cdot \tau_r}{\tau_{eff} - \tau_r}; A_2 = \frac{N_{d0} \cdot \tau_r}{\tau_{eff} - \tau_r}; \tau_1 = \tau_r; \tau_2 = \tau_{eff}, \quad (4-5 (b))$$

where N_{g0} and N_{d0} are the initial carrier numbers at ground and dark states, respectively; for easy comparison, we deliberately let N_g be the form of Eq. 2-1 by

defining the coefficients A_1 and A_2 , and moreover, τ_r and τ_{eff} correspond respectively to τ_1 and τ_2 . In fact, both τ_{spike} and T_{spike} can be directly predicted by setting $A_1 = 0$ which is exactly the moment as the slower part replaces the faster:

$$\tau_{eff} = \tau_r \left(1 + \frac{N_{d0}}{N_{g0}} \right) = \tau_{spike} = 2 \cdot \tau_{hd} \cdot \exp\left(\frac{\Delta_{hd}}{k_B T_{spike}} \right). \quad (4-6)$$

If we plug in $\tau_r = 1$ ns; $\tau_{hd} = 10$ ps; $\Delta_{hd} = 28.7$ meV; $N_{g0} = 0.13$ and $N_{d0} = 0.87$ into Eq. 4-6, we get τ_{spike} to be 7.69 ns with $T_{spike} = 55.9$ K, quite consistent with the numerically solved result, which illustrates the validity of this simplified case.

Most importantly, Eq. 4-5 reveals the role of the additional path; it is obviously shown that the decrease of τ_{eff} enhances the “status” of carrier supplement from dark excitons whereas the role of radiative recombination of the initial bright excitons continues to decline; as τ_{eff} becomes small enough so that A_1 is almost zero, the whole transition is dominated by the relaxation of dark excitons through the additional path which leads to the faster lifetime of the decay PL trace to change from τ_r (τ_1) to τ_{eff} (τ_2). What is more, τ_{eff} actually correlates to both N_{d0} and N_{g0} (Eq. 4-6); due to the long carrier lifetime we observe experimentally, we are forced to assume $N_{d0} \gg N_{g0}$; otherwise, τ_{spike} will be relatively small, for instance, merely 2 ns if $N_{d0} = N_{g0}$.

4.4.2 Discussion on the influences of parameters

The initially given parameters can actually be tuned in a reasonable range, and to demonstrate the roles of them, we now talk about how they have influences on the simulation results. The discussion is classified into three groups: the energy spacing, transition times, and ratio of the initial carriers at ground and dark states; for each group, we show the result with respect to the transition temperatures (T_{spike}) and carrier lifetime at $T = T_{spike}$ (τ_{spike}), and note that except the focused parameter to be a

variable value, others are fixed to be the same as in Table. 4-1.

The change of relaxation time from hot to the dark (τ_{hd}) or ground states (τ_{hg}) will vary T_{spike} but have little influence on τ_{spike} as shown in Fig. 4-10 (a). These points are understandable because besides Δ_{hg} and temperature, τ_{hd} is the other factor related to the degree for dark excitons to jump to hot states (Eq. 4-2); T_{spike} increases as relaxation time is longer since it now needs more thermal energy to achieve the same transition rate of the additional path. As for the spin-flip lifetime ($\tau_{spin-flip}$), which we assumed independent of temperature, we show in Fig. 4-10 (b) that $\tau_{spin-flip}$ will be irrelevant to the results of both T_{spike} and τ_{spike} as long as it reaches a large enough value, which is not hard to perceive if we rethink the behaviors of dark excitons at high temperatures (i.e. $T \geq T_{spike}$). Providing that $\tau_{spin-flip}$ being long enough so that dark excitons have an approximate-zero chance to relax from spin-flip process, it makes no difference if it is still longer since carriers already have no probability to transit from this path. To be more concrete, the slow spin-flip process acts as a high barrier which dark excitons must overcome strenuously at low temperature (long $\tau_{spin-flip}$); however, as temperature rises high enough, dark excitons are able to disregard the barrier and relax through another path, so it turns out that the long $\tau_{spin-flip}$ is unimportant under this circumstance.

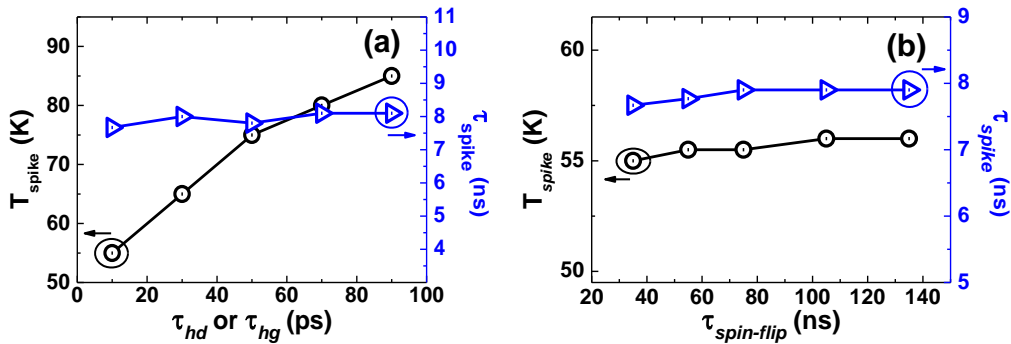


Figure 4-10: Discussions of the parameters: (a) relaxation time from hot to dark state (τ_{hd}) and hot to ground state (τ_{hg}); (b) spin-flip lifetime ($\tau_{spin-flip}$).

In Fig. 4-11 (a) and (b), the discussions center on the energy spacing of the hot to dark state (Δ_{hd}) and ground to dark state (Δ_{gd}), respectively. We first inspect in Fig. 4-11 (a) that the change of Δ_{hd} reveals a shift on T_{spike} , which is understandable; if Δ_{hd} is smaller, carriers need less thermal energy to jump to the hot states (relax through the additional path) and T_{spike} becomes smaller; the result also shows that the variation is quite sensitive between the two where the change of 5 meV in the spacing will lead the T_{spike} to vary about 10 Kelvin. Nevertheless, we do not observe the prediction in our experiment where T_{spike} are nearly the same at 55 K both for sample C and D; we then suspect the responsible reason is that τ_{hg} is a dependent variable of the energy spacing [57] and the overall effect will hold up the change of T_{spike} . In spite of the tight dependence of Δ_{hg} and T_{spike} , τ_{spike} barely changes as Δ_{hg} increases a lot from 15 to 40 meV, which can be comprehended in the following: τ_1 is determined once the temperature rises to the value offering carriers enough probability to relax through the additional path, so τ_1 remains almost a constant due to the same degree of carrier supplement from the path at $T = T_{spike}$. However, compared to Δ_{hd} , Fig. 4-11 (b) tells that Δ_{gd} does not affect either T or τ_{spike} , which is not surprising; the order of Δ_{gd} (~ 0.3 meV) is too small to have an influence on Δ_{hg} (28.7 meV) which determines the capability for carriers to relax through the additional path at a specific temperature.

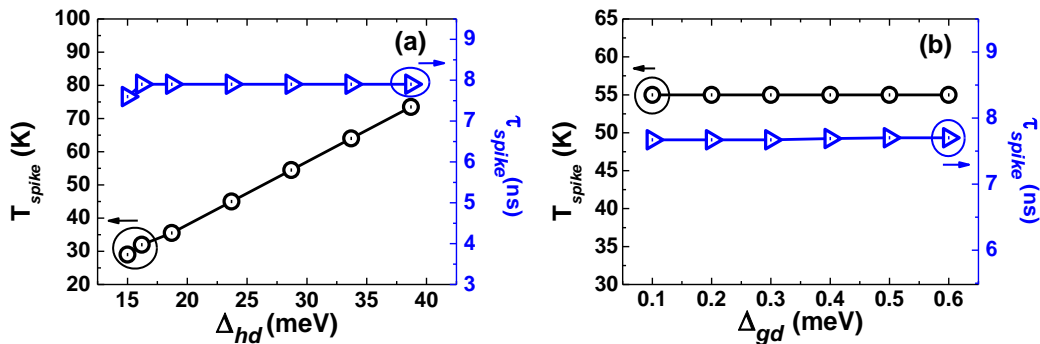


Figure 4-11: Discussion of the parameters of energy spacing between: (a) hot and dark states (Δ_{hd}); (b) ground and dark states (Δ_{gd}).

Finally in Fig. 4-12, the discussion goes to the initial portion of carriers occupying at ground state (G_{gi}). It is evidently observed that to obtain a long τ_{spike} , one must distribute a large amount of carriers initially to dark state, which we previously mentioned in Eq. 4-6. In this case as $T \geq T_{spike}$, there are more carriers coming from the additional path, and the path is like a reservoir to supply carriers to bright state for recombination. If the reservoir is filled with more carriers, it takes a longer time to deplete them to a same extent of portion, leading to a longer carrier lifetime. However, the validity (which we assume) of a small G_{gi} needs further evidences to sustain.

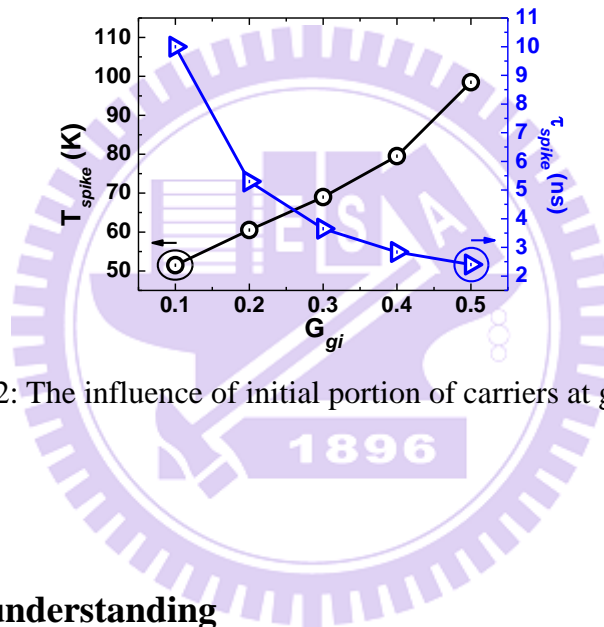


Figure 4-12: The influence of initial portion of carriers at ground state.

A possible misunderstanding

To clarify the meaning of the two carrier lifetimes more specifically, we point out a possible misunderstanding that one may puzzle: as long as there are two exponential decay terms, carriers must be “depleted by two channels”. This is incorrect; as a matter of fact there is only one: the recombination at the very bright state for both bright and dark excitons. The only difference is determined by *how carriers come to the state to recombine*.

The reason why there exists two behaviors in the decaying PL density lies in the rate diversity of the two transition paths. Because of the long spin-flip lifetime, the

speed of carrier supplement from dark to bright state is too slow so that it re-supplies carriers *at a much later time*; as a result, the effect independently reveals *at a much later time* in the time-resolved spectra. In contrast, as temperature is raised high enough so that dark excitons can relax much effectively to bright excitons, the difference between the faster and slower behaviors vanishes since carriers are now injected uninterruptedly to the bright state, causing the two distinct terms to merge.

A short common on the model

Generally speaking, we believe the temperature favors some extra paths for dark excitons to relax in a much easier way back to ground state, but one may be the opinion that it is somewhat trivial as carriers are thermalized. However, we think the proposed idea is quite valuable. The additional path consists a relay level (hot states) for carriers to temporarily stay, and most importantly, the transition is fast enough for carriers not to suffer from relaxation bottleneck; the path remains a non-neglectable role in carrier transitions and its influence will reveal in such a small temperature range.

On the other hand, the model can be further simplified by considering only the dark and bright states and deal with the temperature dependence of transitions from bright (dark) to dark (bright) states. In other words, there may exist other mechanisms and they can be included in the parameters τ_{gd} and τ_{dg} .

4.5 Additional Discussions

Prolonged rising time

We qualitatively showed in the last chapter that the rising time in the decay curves are prolonged to the detectable degree as temperature rises; the simulation also demonstrates a similar result as shown in Fig. 4-13. The theoretical rising time remains 0.26 ns as $T \leq 55$ K and rises to 0.9 ns at 60 Kelvin; it then gradually decreases back to about 0.6 ns at $T = 100$ K. Referring back to Fig. 3-9 (b), the experimental rising time is indeed prolonged at about 65 Kelvin which matches the simulation result.

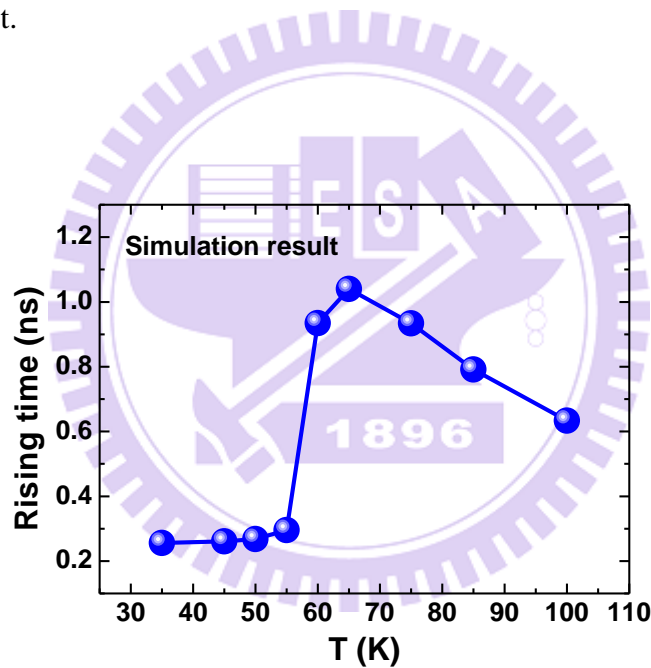


Figure 4-13: Simulation result of the rising time.

Power dependent measurement

It is clearly shown in Fig. 3-6 that the low-T spike will be largely suppressed by high power injection. Although this phenomenon is not focused in the simulation work, we propose a possible explanation qualitatively. Under high power injection,

bi-excitons are more likely to be generated, and it is guaranteed that the excitonic type to which they relax will be bright excitons. As a result, dark excitons are suppressed and so does the spike. However, we did not take the bi-excitonic states into consideration in our model, and it also needs more evidences from both simulation and experiment to support the argument.

4.6 Issues and Limitation

There are some limitations of this model. Firstly, the transition temperature (T_{spike}) should have changed for different sizes of QDs (with different Δ_{hg}), while in experiment we find that $T_{spike} \sim 55$ K for both two samples. Furthermore, for larger QDs with smaller Δ_{hg} , dark excitons should be more capable to relax back to bright excitons through the additional path at lower temperatures, consequently accompanied with a long carrier lifetime, which is not observed, either. Also, to get the τ_1 value at $T = T_{spike}$ as large as in experiment, one must assume that the initial carriers at ground state be nearly zero (Eq. 4-6); in other words, carriers almost all occupy initially at dark states. This is not straightforward since in such a small energy difference, carriers may have an equal probability be captured by either the two.

Chapter 5

Conclusions and Future Studies

We present a first observation on the low-temperature spike of carrier lifetimes in InAs QDs and find out that it will be highly suppressed under high power excitation. The unusual phenomenon is experimentally proved to be very different from the well-known effects at higher temperature; instead, from both the decay curves and fitting parameters we find that the spike is the consequence of the replacement of the faster τ_1 by the slower τ_2 . Furthermore, the spike behavior not only occurs in particular QDs with an intermediate sizes but, however, in some other conditions which we did not find out yet.

Theoretically, we propose a three-level system containing a dark exciton state to explain the observation. For dark excitons to relax to bright states for recombination, the typical process will be the slow spin-flip relaxation, but it is demonstrated that they can relax through an additional path which temperature favors with a much faster rate. The additional path becomes dominating in the whole dynamics system as τ_{eff} is small enough and it results the low-T spike to occur. We also believe that this additional path is a fresh concept for the role of the excited state being as a relay level. This remark may have a critical impact on the realization of further quantum photonics applications or quantum light sources [58], using the advantage of the long-lived exciton spins.

In the future, we prepare to focus on certain aspects. Firstly, the size-dependence issue must be further studied by measuring more samples to have a clear trend that under what conditions will the phenomenon reveal. Second, some other experiments can be done such as the PL polarization measurement and TRPL on more different

detection energies. For theoretical work, the proposed model needs modification; by combining certain fundamental calculations about the temperature-dependent spin-flip dynamics, the parameters in rate equations can be adjusted to further meet the real situation.



Bibliography

- [1] J. W. Kim, et al., "Room temperature far infrared (8~10 μm) photodetectors using self-assembled InAs quantum dots with high detectivity," *IEEE Electron Device Letters*, vol. 21, pp. 329-331, 2000.
- [2] L. Jiang, et al., "In_{0.6}Ga_{0.4}As/GaAs quantum-dot infrared photodetector with operating temperature up to 260 K," *Applied Physics Letters*, vol. 82, pp. 1986-1988, 2003.
- [3] D. Pan, et al., "A five-period normal-incidence (In, Ga)As/GaAs quantum-dot infrared photodetector," *Applied Physics Letters*, vol. 75, pp. 2719-2721, 1999.
- [4] S. J. Xu, et al., "Characteristics of InGaAs quantum dot infrared photodetectors," *Applied Physics Letters*, vol. 73, pp. 3153-3155, 1998.
- [5] P. Werle, "A review of recent advances in semiconductor laser based gas monitors," *Spectrochimica Acta Part a-Molecular and Biomolecular Spectroscopy*, vol. 54, pp. 197-236, 1998.
- [6] A. Schmohl, et al., "Detection of ammonia by photoacoustic spectroscopy with semiconductor lasers," *Applied Optics*, vol. 41, pp. 1815-1823, 2002.
- [7] P. Werle, et al., "Application of antimonide lasers for gas sensing in the 3-4 μm range," *Applied Optics*, vol. 38, pp. 1494-1501, 1999.
- [8] T. Takamoto, et al., "Over 30% efficient InGaP/GaAs tandem solar cells," *Applied Physics Letters*, vol. 70, pp. 381-383, 1997.
- [9] T. Takamoto, et al., "High-efficiency InGaP/In_{0.01}Ga_{0.99}As tandem solar cells lattice-matched to Ge substrates," *Solar Energy Materials and Solar Cells*, vol. 66, pp. 511-516, 2001.
- [10] J. F. Geisz, et al., "High-efficiency GaInP/GaAs/InGaAs triple-junction solar cells grown inverted with a metamorphic bottom junction," *Applied Physics Letters*, vol. 91, p. 023502, 2007.
- [11] N. H. Karam, et al., "Development and characterization of high-efficiency Ga_{0.5}In_{0.5}P/GaAs/Ge dual- and triple-junction solar cells," *IEEE Transactions on Electron Devices*, vol. 46, pp. 2116-2125, 1999.

- [12] M. Grundmann, et al., "Ultrannarrow luminescence lines from single quantum dots," *Physical Review Letters*, vol. 74, pp. 4043-4046, 1995.
- [13] X. D. Huang, et al., "Very low threshold current density room temperature continuous-wave lasing from a single-layer InAs quantum-dot laser," *IEEE Photonics Technology Letters*, vol. 12, pp. 227-229, 2000.
- [14] L. Chu, et al., "Influence of growth conditions on the photoluminescence of self-assembled InAs/GaAs quantum dots," *Journal of Applied Physics*, vol. 85, pp. 2355-2362, 1999.
- [15] K. Mukai, et al., "1.3- μm CW lasing of InGaAs-GaAs quantum dots at room temperature with a threshold current of 8 mA," *IEEE Photonics Technology Letters*, vol. 11, pp. 1205-1207, 1999.
- [16] D. L. Huffaker, et al., "1.3 μm room-temperature GaAs-based quantum-dot laser," *Applied Physics Letters*, vol. 73, pp. 2564-2566, 1998.
- [17] K. Hennessy, et al., "Quantum nature of a strongly coupled single quantum dot-cavity system," *Nature*, vol. 445, pp. 896-899, 2007.
- [18] D. Bimberg, et al., *Quantum Dot Heterostructures*, New York: Wiley, 1998.
- [19] E. A. Stinaff, et al., "Optical signatures of coupled quantum dots," *Science*, vol. 311, pp. 636-639, 2006.
- [20] S. Maimon, et al., "Intersublevel transitions in InAs/GaAs quantum dots infrared photodetectors," *Applied Physics Letters*, vol. 73, pp. 2003-2005, 1998.
- [21] I. P. Marko, et al., "Carrier transport and recombination in p-doped and intrinsic 1.3 μm InAs/GaAs quantum-dot lasers," *Applied Physics Letters*, vol. 87, p. 211114, 2005.
- [22] D. I. Lubyshev, et al., "Exciton localization and temperature stability in self-organized InAs quantum dots," *Applied Physics Letters*, vol. 68, pp. 205-207, 1996.
- [23] W. D. Yang, et al., "Effect of carrier emission and retrapping on luminescence time decays in InAs/GaAs quantum dots," *Physical Review B*, vol. 56, pp. 13314-13320, 1997.

- [24] L. Zhang, et al., "Dynamic response of 1.3- μm -wavelength InGaAs/GaAs quantum dots," *Applied Physics Letters*, vol. 76, pp. 1222-1224, 2000.
- [25] R. Heitz, et al., "Temperature dependent optical properties of self-organized InAs/GaAs quantum dots," *Journal of Electronic Materials*, vol. 28, pp. 520-527, 1999.
- [26] S. Sanguinetti, et al., "Carrier thermal escape and retrapping in self-assembled quantum dots," *Physical Review B*, vol. 60, p. 8276, 1999.
- [27] S. Sanguinetti, et al., "Temperature dependence of the photoluminescence of InGaAs/GaAs quantum dot structures without wetting layer," *Applied Physics Letters*, vol. 81, pp. 3067-3069, 2002.
- [28] W. H. Chang, et al., "Photocurrent studies of the carrier escape process from InAs self-assembled quantum dots," *Physical Review B*, vol. 62, pp. 6959-6962, 2000.
- [29] A. M. Adawi, et al., "Comparison of intraband absorption and photocurrent in InAs/GaAs quantum dots," *Applied Physics Letters*, vol. 83, pp. 602-604, 2003.
- [30] M. Gurioli, et al., "Recombination kinetics of InAs quantum dots: Role of thermalization in dark states," *Physical Review B*, vol. 73, p. 085302, 2006.
- [31] F. Adler, et al., "Optical transitions and carrier relaxation in self assembled InAs/GaAs quantum dots," *Journal of Applied Physics*, vol. 80, pp. 4019-4026, 1996.
- [32] R. Heitz, et al., "Excited states and energy relaxation in stacked InAs/GaAs quantum dots," *Physical Review B*, vol. 57, p. 9050, 1998.
- [33] J. Shah, *Ultrafast Spectroscopy of Semiconductors and Semiconductor Nanostructures*: Springer, 1999.
- [34] A. Othonos, "Probing ultrafast carrier and phonon dynamics in semiconductors," *Journal of Applied Physics*, vol. 83, pp. 1789-1830, 1998.
- [35] M. Wahl, "Time-Correlated Single Photon Counting."
- [36] J. M. Moison, et al., "Self-organized growth of regular nanometer-scale InAs dots on GaAs," *Applied Physics Letters*, vol. 64, pp. 196-198, 1994.

- [37] D. Leonard, et al., "Critical layer thickness for self-assembled InAs islands on GaAs," *Physical Review B*, vol. 50, p. 11687, 1994.
- [38] P. M. Petroff, et al., "MBE and MOCVD growth and properties of self-assembling quantum-dot arrays in III-V semiconductor structures," *Superlattices and Microstructures*, vol. 15, pp. 15-21, 1994.
- [39] D. Leonard, et al., "Direct formation of quantum-sized dots from uniform coherent islands of InGaAs on GaAs-surfaces," *Applied Physics Letters*, vol. 63, pp. 3203-3205, 1993.
- [40] M. Bayer, et al., "Fine structure of neutral and charged excitons in self-assembled In(Ga)As/(Al)GaAs quantum dots," *Physical Review B*, vol. 65, p. 195315, 2002.
- [41] A. V. Khaetskii, et al., "Spin-flip transitions between Zeeman sublevels in semiconductor quantum dots," *Physical Review B*, vol. 64, p. 125316, 2001.
- [42] I. A. Merkulov, et al., "Electron spin relaxation by nuclei in semiconductor quantum dots," *Physical Review B*, vol. 65, p. 205309, 2002.
- [43] A. V. Khaetskii, et al., "Electron spin decoherence in quantum dots due to interaction with nuclei," *Physical Review Letters*, vol. 88, p. 186802, 2002.
- [44] E. Tsitsishvili, et al., "Exciton-spin relaxation in quantum dots due to spin-orbit interaction," *Physical Review B*, vol. 72, p. 155333, 2005.
- [45] K. Roszak, et al., "Exciton spin decay in quantum dots to bright and dark states," *Physical Review B*, vol. 76, p. 195324, 2007.
- [46] J. Johansen, et al., "Probing long-lived dark excitons in self-assembled quantum dots," *Physical Review B*, vol. 81, p. 081304, 2010.
- [47] M. Reischle, et al., "Influence of the dark exciton state on the optical and quantum optical properties of single quantum dots," *Physical Review Letters*, vol. 101, p. 4, 2008.
- [48] Y.-H. Liao, et al., "Dominant channels of exciton spin relaxation in photoexcited self-assembled (In,Ga)As quantum dots," *Physical Review B*, vol. 83, p. 165317, 2011.
- [49] J. Urayama, et al., "Observation of Phonon Bottleneck in Quantum Dot

- Electronic Relaxation," *Physical Review Letters*, vol. 86, pp. 4930-4933, 2001.
- [50] R. Heitz, et al., "Existence of a phonon bottleneck for excitons in quantum dots," *Physical Review B*, vol. 64, p. 241305, 2001.
- [51] U. Woggon, et al., "Ultrafast energy relaxation in quantum dots," *Physical Review B*, vol. 54, p. 17681, 1996.
- [52] S. Sanguinetti, et al., "Role of the wetting layer in the carrier relaxation in quantum dots," *Applied Physics Letters*, vol. 81, pp. 613-615, 2002.
- [53] B. Ohnesorge, et al., "Rapid carrier relaxation in self-assembled $\text{In}_x\text{Ga}_{1-x}\text{As}/\text{GaAs}$ quantum dots," *Physical Review B*, vol. 54, p. 11532, 1996.
- [54] T. S. Sosnowski, et al., "Rapid carrier relaxation in $\text{In}_{0.4}\text{Ga}_{0.6}\text{As}/\text{GaAs}$ quantum dots characterized by differential transmission spectroscopy," *Physical Review B*, vol. 57, pp. R9423-R9426, 1998.
- [55] R. Heitz, et al., "Energy relaxation by multiphonon processes in InAs/GaAs quantum dots," *Physical Review B*, vol. 56, pp. 10435-10445, 1997.
- [56] E. Tsitsishvili, et al., "Exciton spin relaxation in strongly confining semiconductor quantum dots," *Physical Review B*, vol. 82, p. 195315, 2010.
- [57] H. Htoon, et al., "Carrier relaxation and quantum decoherence of excited states in self-assembled quantum dots," *Physical Review B*, vol. 63, p. 241303, 2001.
- [58] A. J. Shields, "Semiconductor quantum light sources," *Nature Photonics*, vol. 1, pp. 215-223, 2007.

Vita

Name: Chun Cheng (鄭濬)

Sex: Male

Date of birth: 10th May 1987

Nationality: Republic of China (Taiwan)

Education:

M.S. (2009. 9 – 2011. 6)

Department of Electronics Engineering, National Chiao Tung University

B.S. (2005. 9 – 2009. 6)

Department of Electrophysics, National Chiao Tung University

Title of Master Thesis:

Temperature-Dependent Carrier Dynamics of InAs/GaAs Quantum Dots

